

The Chandra Cosmos Legacy Survey: Overview and Point Source Catalog

Civano, F.; Marchesi, S.; Comastri, A.; Urry, M. C.; Elvis, M.; Cappelluti, N.; Puccetti, S.; Brusa, M.; Zamorani, G.; Hasinger, G.; ...

Source / Izvornik: **Astrophysical Journal**, 2016, 819, 62 - 80

Journal article, Published version

Rad u časopisu, Objavljena verzija rada (izdavačev PDF)

<https://doi.org/10.3847/0004-637X/819/1/62>

Permanent link / Trajna poveznica: <https://urn.nsk.hr/urn:nbn:hr:217:968544>

Rights / Prava: [In copyright](#) / [Zaštićeno autorskim pravom.](#)

Download date / Datum preuzimanja: **2025-03-25**



Repository / Repozitorij:

[Repository of the Faculty of Science - University of Zagreb](#)



THE *CHANDRA* COSMOS LEGACY SURVEY: OVERVIEW AND POINT SOURCE CATALOG

F. CIVANO^{1,2}, S. MARCHESI^{1,2,3}, A. COMASTRI⁴, M. C. URRY¹, M. ELVIS², N. CAPPELLUTI⁴, S. PUCCEITI⁵, M. BRUSA^{3,4},
 G. ZAMORANI⁴, G. HASINGER⁶, T. ALDCROFT², D. M. ALEXANDER⁷, V. ALLEVATO⁸, H. BRUNNER⁹, P. CAPAK^{10,11}, A. FINOGUENOV⁸,
 F. FIORE¹², A. FRUSCIONE², R. GILLI⁴, K. GLOTFELTY², R. E. GRIFFITHS¹³, H. HAO², F. A. HARRISON¹⁴, K. JAHNKE¹⁵,
 J. KARTALTEPE^{16,17}, A. KARIM¹⁸, S. M. LAMASSA¹, G. LANZUISI^{3,4}, T. MIYAJI^{19,20}, P. RANALLI²¹, M. SALVATO⁹, M. SARGENT²²,
 N. J. SCOVILLE¹¹, K. SCHAWINSKI²³, E. SCHINNERER^{15,24}, J. SILVERMAN²⁵, V. SMOLCIC²⁶, D. STERN²⁷, S. TOFT²⁸,
 B. TRAKHENBROT²³, E. TREISTER²⁹, AND C. VIGNALI^{3,4}

¹ Yale Center for Astronomy and Astrophysics, 260 Whitney Avenue, New Haven, CT 06520, USA

² Harvard-Smithsonian Center for Astrophysics, 60 Garden Street, Cambridge, MA 02138, USA

³ Dipartimento di Fisica e Astronomia, Università di Bologna, viale Bertini Pichat 6/2, I-40127 Bologna, Italy

⁴ INAF—Osservatorio Astronomico di Bologna, via Ranzani 1, I-40127 Bologna, Italy

⁵ ASDC—ASI, Via del Politecnico, I-00133 Roma, Italy

⁶ Institute for Astronomy, 2680 Woodlawn Drive, University of Hawaii, Honolulu, HI 96822, USA

⁷ Centre for Extragalactic Astronomy, Department of Physics, Durham University, South Road, Durham DH1 3LE, UK

⁸ Department of Physics, University of Helsinki, Gustaf Hällströmin katu 2a, FI-00014 Helsinki, Finland

⁹ Max-Planck-Institut für extraterrestrische Physik, Giessenbachstrasse 1, D-85748 Garching bei München, Germany

¹⁰ Infrared Processing and Analysis Center (IPAC), 1200 East California Boulevard, Pasadena, CA 91125, USA

¹¹ California Institute of Technology, 1200 East California Boulevard, Pasadena, CA 91125, USA

¹² INAF—Osservatorio Astronomico di Roma, via Frascati 33, Monte Porzio Catone, I-00040, Italy

¹³ Physics & Astronomy Dept., Natural Sciences Division, University of Hawaii at Hilo, 200 W. Kawili St., Hilo, HI 96720, USA

¹⁴ Cahill Center for Astronomy and Astrophysics, California Institute of Technology, 1216 E. California Blvd, Pasadena, CA 91125 USA

¹⁵ Max Planck Institute for Astronomy, Königstuhl 17, D-69117 Heidelberg, Germany

¹⁶ National Optical Astronomy Observatory, 950N. Cherry Ave, Tucson AZ 85719, USA

¹⁷ School of Physics and Astronomy, Rochester Institute of Technology, 84 Lomb Memorial Dr., Rochester, NY 14623, USA

¹⁸ Argelander-Institut für Astronomie, Universität Bonn, Auf dem Hügel 71, D-53121 Bonn, Germany

¹⁹ Instituto de Astronomía sede Ensenada, Universidad Nacional Autónoma de México, Km. 103, Carret. Tijuana-Ensenada, Ensenada, BC, Mexico

²⁰ University of California San Diego, Center for Astrophysics and Space Sciences, 9500 Gilman Drive, La Jolla, CA 92093-0424, USA

²¹ AASARS, National Observatory of Athens, 15236 Penteli, Greece

²² Astronomy Centre, Department of Physics and Astronomy, University of Sussex, Brighton, BN1 9QH, UK

²³ Institute for Astronomy, Department of Physics, ETH Zurich, Wolfgang-Pauli-Strasse 27, CH-8093 Zurich, Switzerland

²⁴ National Radio Astronomy Observatory, Pete V. Domenici Science Operations Center, 1003 Lopezville Road, Socorro, NM 87801, USA

²⁵ Kavli Institute for the Physics and Mathematics of the universe (Kavli IPMU, WPI), Todai Institutes for Advanced Study, The University of Tokyo, Kashiwa 277-8583, Japan

²⁶ Department of Physics, University of Zagreb, Bijenička cesta 32, HR-10000 Zagreb, Croatia

²⁷ Jet Propulsion Laboratory, California Institute of Technology, 4800 Oak Grove Drive, Pasadena, CA 91109, USA

²⁸ Dark Cosmology Centre, Niels Bohr Institute, University of Copenhagen, Juliane Mariesvej 30, DK-2100 Copenhagen, Denmark

²⁹ Universidad de Concepción, Departamento de Astronomía, Casilla 160-C, Concepción, Chile

Received 2015 July 31; accepted 2015 December 24; published 2016 February 29

ABSTRACT

The *COSMOS-Legacy* survey is a 4.6 Ms *Chandra* program that has imaged 2.2 deg² of the COSMOS field with an effective exposure of $\simeq 160$ ks over the central 1.5 deg² and of $\simeq 80$ ks in the remaining area. The survey is the combination of 56 new observations obtained as an X-ray Visionary Project with the previous C-COSMOS survey. We describe the reduction and analysis of the new observations and the properties of 2273 point sources detected above a spurious probability of 2×10^{-5} . We also present the updated properties of the C-COSMOS sources detected in the new data. The whole survey includes 4016 point sources (3814, 2920 and 2440 in the full, soft, and hard band). The limiting depths are 2.2×10^{-16} , 1.5×10^{-15} , and 8.9×10^{-16} erg cm⁻² s⁻¹ in the 0.5–2, 2–10, and 0.5–10 keV bands, respectively. The observed fraction of obscured active galactic nuclei with a column density $> 10^{22}$ cm⁻² from the hardness ratio (HR) is $\sim 50_{-16}^{+17}\%$. Given the large sample we compute source number counts in the hard and soft bands, significantly reducing the uncertainties of 5%–10%. For the first time we compute number counts for obscured (HR > -0.2) and unobscured (HR < -0.2) sources and find significant differences between the two populations in the soft band. Due to the unprecedented large exposure, *COSMOS-Legacy* area is three times larger than surveys at similar depths and its depth is three times fainter than surveys covering similar areas. The area-flux region occupied by *COSMOS-Legacy* is likely to remain unsurpassed for years to come.

Key words: catalogs – cosmology: observations – galaxies: evolution – quasars: general – surveys – X-rays: general

Supporting material: machine-readable table

1. INTRODUCTION

One of the most active but least-known epochs in astrophysics is the period between reionization ($z \gtrsim 8$, i.e.,

when the universe was less than ~ 0.6 Gyr old), where the growth of structures becomes highly nonlinear and the first stars form, and $z \sim 2$ (~ 3.25 Gyr old), where major

virialization occurs and star formation (SF) and supermassive black hole (SMBH) accretion peak.

At these early times the precursors of the clusters and groups seen at $z \lesssim 1$ have low density and are much larger on both physical (Mpc) and observed (arcminutes) scales. Surveys for these large-scale structures become rapidly more efficient as the dimension of the survey exceeds the structure's typical sizes ($\sim 15'$). Large area surveys (several times $15'$ wide) are essential for the detection of these structures, which cannot be seen in smaller area surveys, however deep.

The equatorial 2 deg^2 COSMOS area (Scoville et al. 2007a) is the deepest, most complete survey accessible to both hemispheres (notably by both ALMA and the Karl G. Jansky VLA) and is large enough to find high redshift clusters. A significant investment of 640 *Hubble Space Telescope* (HST) orbits (Koekemoer et al. 2007, Scoville et al. 2007b), 620h of *Spitzer* (P. Capak et al. 2016, in preparation³⁰), 260h of *Herschel* (Lutz et al. 2011), 750 hr of JVLA (Schinnerer et al. 2004, 2007, 2010 and V. Smolcic et al. 2016 in preparation), over 300 nights of large ground-based telescopes VLT, Keck, Subaru, VISTA for both imaging and spectroscopy (Taniguchi et al. 2007; Lilly et al. 2009) have been made in this field.

The first homogeneous coverage in the X-rays of the whole COSMOS field was obtained with the *XMM-Newton* satellite (1.5 Ms; Hasinger et al. 2007; Cappelluti et al. 2009; Brusa et al. 2010). These observations have been crucial for characterizing the most luminous Active Galactic Nuclei (AGNs) in COSMOS (e.g., Brusa et al. 2010; Alleinato et al. 2011; Mainieri et al. 2011; Lusso et al. 2012 among others). The obscured AGN population of the COSMOS field can be studied by jointly using the XMM-COSMOS data with the ~ 3 Ms of *NuSTAR* (Harrison et al. 2012) time available, which led to the discovery of a Compton-thick AGN (with obscuration exceeding 10^{24} cm^{-2} equivalent hydrogen column density) in the field (Civano et al. 2015) that was not recognized as such by *XMM-Newton* alone. Instead, for the faint and the high- z AGN population that could be responsible for the reionization of the universe (see Giallongo et al. 2015), *Chandra* (Weisskopf et al. 2002) is the preferred instrument. Indeed, the large (1.8 Ms) *Chandra* COSMOS survey (C-COSMOS; Elvis et al. 2009, E09; Puccetti et al. 2009, P09; Civano et al. 2012) has already contributed significantly to the study of the early epochs of the universe with the following findings: three luminous AGN residing in protoclusters between $z \sim 4.55$ and 5.3 (Capak et al. 2011); the largest sample of X-ray selected $z > 3$ quasars in a contiguous field (81 sources, Civano et al. 2011); a precocious SMBH in a normal-sized galaxy at $z > 3$ (Trakhtenbrot et al. 2015); and AGN correlation lengths of $7h^{-1} \text{ Mpc}$ ($\sim 10'$) at $z \sim 1-2$, Alleinato et al. 2011). However, C-COSMOS only covered $\frac{1}{4}$ of COSMOS at $\sim 160 \text{ ks}$ depth plus 0.5 deg^2 at $\sim 80 \text{ ks}$ depth (Figure 1, green squares).

We present here the *Chandra* COSMOS-Legacy survey³¹, which is the combination of the old C-COSMOS survey with 2.8 Ms of new *Chandra* ACIS-I (Garmire et al. 2003) observations ($56 \times 50 \text{ ks}$ pointings) approved during *Chandra* Cycle 14 as an X-ray Visionary Project (PI: F. Civano; program

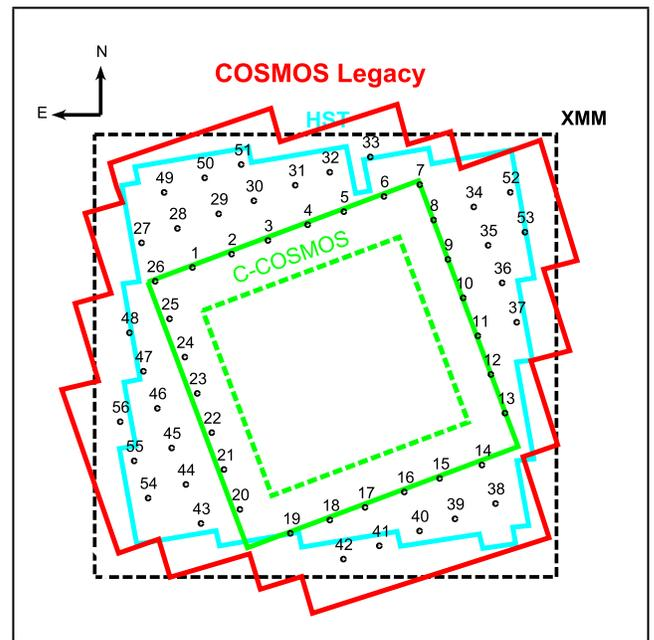


Figure 1. *COSMOS-Legacy* tiling (red) compared to the area covered by *HST* (cyan), C-COSMOS (green solid: total area; green dashed: deeper area), and XMM-COSMOS (black). The ordering numbers of new observations are marked (see Table 1).

ID 901037). *COSMOS-Legacy* uniformly covers the $\sim 1.7 \text{ deg}^2$ COSMOS/*HST* field at $\sim 160 \text{ ks}$ depth, expanding on the deep C-COSMOS area (dashed green square in Figure 1) by a factor of ~ 3 at $\sim 3 \times 10^{-16} \text{ erg cm}^{-2} \text{ s}^{-1}$ (1.45 versus 0.44 deg^2), for a total area covered of $\sim 2.2 \text{ deg}^2$.

This paper is the first in a series and presents the main properties of the survey and the X-ray point source catalog to be followed by a paper on the multiwavelength identification of the X-ray sources by Marchesi et al. (2016). In Section 2 we present the observations and tiling strategy. In Section 3 we detail all the steps of the data processing including astrometric corrections, exposure, and background map production. The data analysis procedure is instead described in Section 4 with some references and comparison with the one adopted for C-COSMOS as explained in P09. The point source catalog and the source properties are presented in Section 4.1. Sections 5 and 6 present the survey sensitivity and the number counts in both soft and hard bands and divide the sources into obscured and unobscured.

We assume a cosmology with $H_0 = 71 \text{ km s}^{-1} \text{ Mpc}^{-1}$, $\Omega_M = 0.3$ and $\Omega_\Lambda = 0.7$, and magnitudes are reported in the AB system if not otherwise stated. Throughout this paper, we make use of J2000.0 coordinates. The data analysis is performed in three X-ray bandpasses 0.5–2 keV (soft band, S), 2–7 keV (hard band, H), and 0.5–7 keV (full band, F), while sensitivity and fluxes have been computed in the 0.5–2, 2–10 and 0.5–10 keV bands for an easy comparison with other works in the literature.

2. OBSERVATIONS

The half-a-field shift tiling strategy was designed to uniformly cover the COSMOS *Hubble* area in depth and point-spread function (PSF) size (cyan outline in Figure 1; Scoville et al. 2007b) by combining the old C-COSMOS observations (green outline in Figure 1) with the new *Chandra* ones (red outline in Figure 1). To achieve this 56, ACIS-I

³⁰ See the SPLASH survey website at <http://splash.caltech.edu/>.

³¹ Throughout the paper we use the term C-COSMOS to refer to the original survey of the inner field, and the name *Chandra* COSMOS-Legacy survey to refer to the full combined survey including the new data presented here.

pointings (numbered black points in Figure 1) were used, 11 of which were scheduled as two or more separate observations because of satellite constraints, for a total of 68 pointings. Moreover, the observing roll angle was constrained to be within 70 ± 20 degrees or 250 ± 20 . We summarize the main properties of the new *Chandra* COSMOS-Legacy observations in Table 1.

The observations took place in four blocks: 2012 November to 2013 January; 2013 March to July; 2013 October to 2014 January; and 2014 March. The mean net effective exposure time per field was 48.8 ks after all the cleaning and reduction operations (see Section 4). The maximum exposure was 53 ks (observation 15227) while the minimum exposure was 45.2 ks (combined observations 15208 and 15998).

The sequence of the observations was designed to start from the N–E top corner tile of C-COSMOS, move toward W, and proceed clockwise around the central C-COSMOS area in such a way that the outer frame of the C-COSMOS survey overlaps with the inner frame of the new *Chandra* observations. The tiling number and the total area covered is shown in Figure 1.

Using this tiling strategy we achieve an approximately uniform combined PSF across the survey. The mean combined PSF width (size at 50% of the encircled energy fraction, EE_F, in the 0.5–7 keV band; see Section 5 for details on the PSF maps) weighted on the exposure peaks at around 3" (see Figure 2). As shown in Figure 2, 80% of the field has a PSF in the range 2"–4". As a comparison, in a single-pointed survey (regardless of exposure time) the PSF size distribution is flat, and although ~30% of the field has a PSF <2" it can reach a substantially larger size (>4") in 40% of the field.

3. DATA PROCESSING

The data reduction was performed following the procedures described in E09 for C-COSMOS using standard *Chandra* CIAO 4.5 tools (Fruscione et al. 2006) and CALDB 4.5.9. We also reprocessed the 49 C-COSMOS observations to use them in concert with the new observations for source detection in the area where the new observations overlap with the old ones and to compute the sensitivity of the whole survey (see the comparison between fluxes in Section 4.1.3).

We used the `chandra_repro` reprocessing script, which automates the CIAO recommended data processing steps and creates new level 2 event files, and applied the *VFAINT* mode for ACIS background cleaning to all the observations. We then performed the following steps before starting data analysis: astrometric correction and reprocessing of all the observations to a standard frame of reference using the new aspect solution (Section 3.1); mosaic and exposure map creation in three standard *Chandra* bands (Section 3.2): 0.5–7 keV, 0.5–2 keV and 2–7 keV; background map creation using a two-components model to take into account both the cosmic background contribution and the instrumental one (Section 3.3).

3.1. Astrometric Corrections

Even though *Chandra* data astrometry is accurate to 0".6 (at 90% confidence, see Proposer User Guide³² Chapter 5), to produce a sharp X-ray mosaic and to match the positions of X-ray sources with the optical catalog for which the positional accuracy is ~0".2 (Capak et al. 2007; Ilbert et al. 2009; Laigle

et al. submitted), we performed source detection on each individual observation to register them to a common optical astrometric frame. This work has been done on the new observations and also on the C-COSMOS outer frame fields and was overlapping with the new data. We generated a list of detected sources using the CIAO wavelet source detection tool `WAVDETECT` on each single observation binned at 1" and adopted a false-positive detection probability threshold corresponding to ~10 spurious sources per field. Of the detected sources (on average 150 sources per field) we considered in each field those with significance $>3.5\sigma$ and within 360" from the aim point. In *Chandra* data the positional accuracy of significant sources is <1" even at 10' off-axis and it is energy-independent (K. Glotfelty 2015, private communication). Therefore, choosing sources within 6' of the aim point provides a sample of sources with a very good centroid estimate (<0".3) for astrometric purposes. Using the CIAO tool `reproject_aspect`, these sources were then compared with the CFHT *MegaCam* catalog of i-band-selected sources (McCracken et al. 2012) with optical magnitudes in the range 18–23 AB mag. At least four sources in each field, that are not on the same side of the aim point, are needed to compute meaningful rotational and translation transformations. In our analysis we used on average 12 sources (up to 22 sources per field) with 75% of the fields having more than 10 sources used to perform the reprojection.

With the corrected aspect solution we reprocessed the level 1 data using `chandra_repro` and performed the `WAVDETECT` detection again to compute the new separation between X-ray and optical positions. The resulting standard deviation on the shift computed from the detected sources within 6' is 0".36 and 0".51 on the R.A. and decl., respectively. After matching all the X-ray fields to the same astrometric optical frame, 95% of the X-ray sources used for the astrometry correction have a distance to their optical counterpart smaller than 1".4, 10% lower than the value before the correction (1".53). The improvement in the position increases to 20% when considering 90% of the sources (1".26 to 1".02) and 30% when considering a smaller sample of 68% of the sources (from 0".72 to 0".51; see Figure 3). This is consistent with and slightly better than what was found for C-COSMOS (see E09, Figure 6).

3.2. Exposure Maps and Data Mosaic Creation

We created exposure maps in three bands using the standard CIAO procedure. The spectral model used for the map creation is a single power-law with a slope of $\Gamma = 1.4$ ³³ and Galactic absorption of $N_H = 2.6 \times 10^{20} \text{ cm}^{-2}$ (Kalberla et al. 2005). Instrument maps generated with `MKINSTMAP` for each CCD in each observation were used as input files for the `MKEXPMAP` tool, which computes an exposure map for each CCD separately. These exposure maps were combined in a single exposure map for each observation using `DMREGRID` with a binning of 2 pixels.

Figure 4 shows a composite image of the effective exposure time (in seconds) in the full band for both the new observations (left) and the whole *COSMOS-Legacy* (right). As can be seen,

³³ The choice of such a spectral slope is not only because of consistency with E09 and P09, but it is also the slope of the cosmic X-ray background (e.g., Hickox & Markevitch 2006) and therefore well represents a mixed distribution of obscured and unobscured sources at the fluxes covered by *COSMOS-Legacy*.

³² http://cxc.cfa.harvard.edu/proposer/POG/html/chap5.html#tth_flg5.5

Table 1
COSMOS-Legacy Survey (CLS) Observation Summary

Field ^a	Obs. ID	R.A.	Decl.	Date	Exp. Time (s)	Roll (deg)
CLS_1	15207	150.544451	2.499045	2012 Nov 25	14883	70.2
	15590	150.544402	2.499094	2012 Nov 23	14893	70.2
	15591	150.544454	2.499065	2012 Nov 25	19828	70.2
CLS_2	15208	150.415643	2.543225	2012 Dec 07	22985	70.2
	15598	150.415625	2.543213	2012 Dec 08	22193	70.2
CLS_3	15209	150.295749	2.588083	2012 Dec 03	23775	70.2
	15600	150.295747	2.588106	2012 Dec 05	21795	70.2
CLS_4	15604	150.164741	2.639752	2012 Dec 10	20988	70.2
	15210	150.164738	2.639709	2012 Dec 16	24365	70.2
CLS_5	15211	150.045569	2.682903	2012 Dec 13	23572	70.2
	15605	150.045586	2.682879	2012 Dec 15	21801	70.2
CLS_6	15212	149.913425	2.732850	2012 Dec 21	25249	70.2
	15606	149.913418	2.732845	2012 Dec 23	25219	70.2
CLS_7	15213	149.796052	2.772968	2013 Jan 01	49435	62.2
CLS_8	15214	149.751287	2.655331	2013 Jan 03	45983	61.75
CLS_9	15215	149.704144	2.525446	2013 Jan 07	49437	63.2
CLS_10	15216	149.654208	2.399733	2013 Jan 16	46459	56.7
CLS_11	15217	149.627509	2.272922	2013 Mar 23	46057	265.2
CLS_12	15218	149.584767	2.145874	2013 Mar 22	46475	265.2
CLS_13	15219	149.538688	2.017596	2013 Mar 30	49432	261.6
CLS_14	15220	149.614659	1.846399	2013 Apr 04	49924	60.1
CLS_15	15221	149.753949	1.801935	2013 Apr 10	49431	58.2
CLS_16	15222	149.870306	1.757718	2013 Apr 04	49407	60.0
CLS_17	15223	149.999623	1.706079	2013 Apr 17	50905	55.2
CLS_18	15224	150.115609	1.664373	2013 Apr 19	49426	55.2
CLS_19	15225	150.245495	1.621716	2013 Apr 05	49631	59.8
CLS_20	15226	150.411336	1.697830	2013 Jun 21	49428	250.2
CLS_21	15227	150.463753	1.829216	2013 May 02	53051	50.2
CLS_22	15228	150.504029	1.950647	2013 Apr 30	49432	50.2
CLS_23	15229	150.551660	2.080265	2013 May 10	49012	52.2
CLS_24	15230	150.592692	2.199969	2013 May 08	49429	52.2
CLS_25	15231	150.642972	2.325853	2013 May 13	48446	51.0
CLS_26	15232	150.690403	2.449284	2013 May 16	35085	50.6
	15649	150.690409	2.449315	2013 Jun 03	15251	50.65
CLS_27	15233	150.734924	2.575875	2013 May 21	46476	50.20
CLS_28	15234	150.616710	2.623373	2013 May 22	5439	50.20
	15653	150.594589	2.629150	2014 Jan 16	44895	58.21
CLS_29	15235	150.480833	2.671101	2013 Jun 01	49440	48.31
CLS_30	15236	150.364822	2.714260	2013 Jun 01	49435	48.23
CLS_31	15237	150.228563	2.765929	2013 Jun 08	25246	50.65
	15655	150.228550	2.765907	2013 Jun 10	24466	50.65
CLS_32	15238	150.114727	2.808579	2013 Jun 09	49429	50.65
CLS_33	15239	149.981160	2.858739	2013 Jun 11	49430	50.20
CLS_34	15240	149.617459	2.695912	2013 Oct 15	48450	77.09
CLS_35	15241	149.593992	2.566795	2014 Mar 28	48600	260.21
CLS_36	15242	149.547344	2.443553	2013 Jun 22	49432	50.20
CLS_37	15243	149.499113	2.312060	2013 Jul 05	47985	50.20
CLS_38	15244	149.547442	1.723759	2014 Jan 21	47461	53.21
CLS_39	15245	149.680897	1.673516	2014 Jan 23	49437	53.21
CLS_40	15246	149.796705	1.629086	2013 Oct 22	48850	75.21
CLS_41	15247	149.953115	1.578784	2014 Mar 18	49545	267.21
CLS_42	15248	150.047419	1.537353	2013 Nov 13	49438	71.61
CLS_43	15249	150.516513	1.655025	2013 Nov 29	45635	70.21
CLS_44	15250	150.566083	1.783479	2013 Dec 12	49315	70.21
CLS_45	15251	150.612991	1.904134	2013 Dec 03	29702	67.91
	16544	150.613008	1.904121	2013 Dec 04	19830	67.91
CLS_46	15252	150.660018	2.034094	2013 Dec 14	49434	70.21
CLS_47	15253	150.707972	2.162869	2014 Jan 28	49132	53.21
CLS_48	15254	150.753963	2.289683	2014 Jan 29	49139	53.21
CLS_49	15255	150.661405	2.741395	2014 Mar 24	49435	260.21
CLS_50	15256	150.504801	2.795740	2014 Jan 13	49943	59.21
CLS_51	15257	150.384246	2.838987	2014 Jan 04	49435	61.85
CLS_52	15258	149.497504	2.746858	2014 Jan 01	49432	62.27

Table 1
(Continued)

Field ^a	Obs. ID	R.A.	Decl.	Date	Exp. Time (s)	Roll (deg)
CLS_53	15259	149.451159	2.620733	2014 Jan 27	49435	53.21
CLS_54	15260	150.690908	1.740589	2014 Jan 05	22793	60.21
	16562	150.690921	1.740576	2014 Jan 25	26736	60.21
CLS_55	15261	150.736977	1.863191	2014 Jan 18	46474	59.21
CLS_56	15262	150.782957	1.992193	2014 Jan 12	50236	59.21

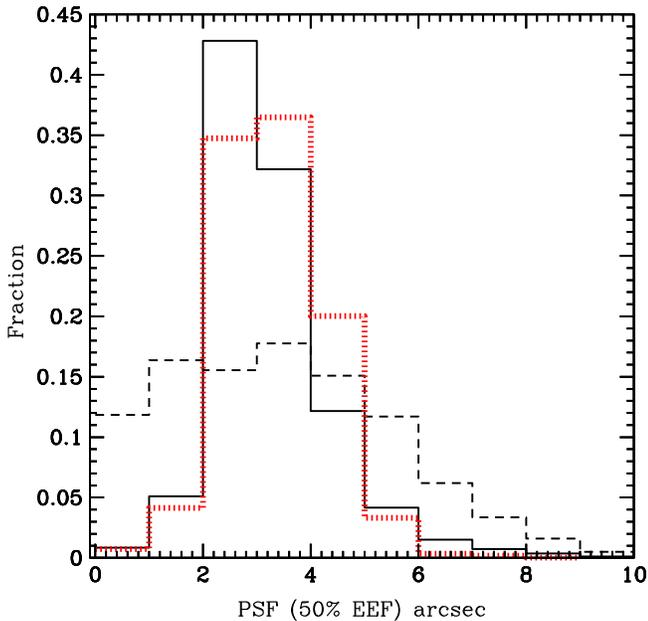


Figure 2. Normalized distribution of the combined point-spread function (50% of EEF in 0.5–7 keV) size in arcseconds measured in *COSMOS-Legacy* (solid histogram) and in a single-pointing survey (dashed line). Red indicates the distribution of the combined PSF (the mean value) for all the detected sources.

the central 1.5 deg^2 covers almost the entire *HST* area and has a uniform depth of $\approx 160 \text{ ks}$.

The data mosaic image was created in three bands using the HEASoft `add images` tool which adds together a set of images using sky coordinates. Figure 5 shows the three-colored image that was created by combining the exposure-corrected images in three non-overlapping bands (0.5–2.0 keV, 2.0–4.5 keV, and 4.5–7.0 keV as red, green, and blue, respectively). The combined image was then Gaussian smoothed with a 3 pixel radius. A filter was then applied to isolate the sources from the background level as well as to increase the contrast and color vibrancy of those sources. This process was repeated three times.

3.3. Background Maps Creation

The *Chandra* background consists of two different components: the cosmic X-ray background and a quiescent instrumental background due to interactions between the ACIS-I CCD detectors and high-energy particles. We followed the procedure described in Cappelluti et al. (2013) to create background maps which we used for the selection of reliable sources in our detection procedure and for the computation of the sensitivity curves.

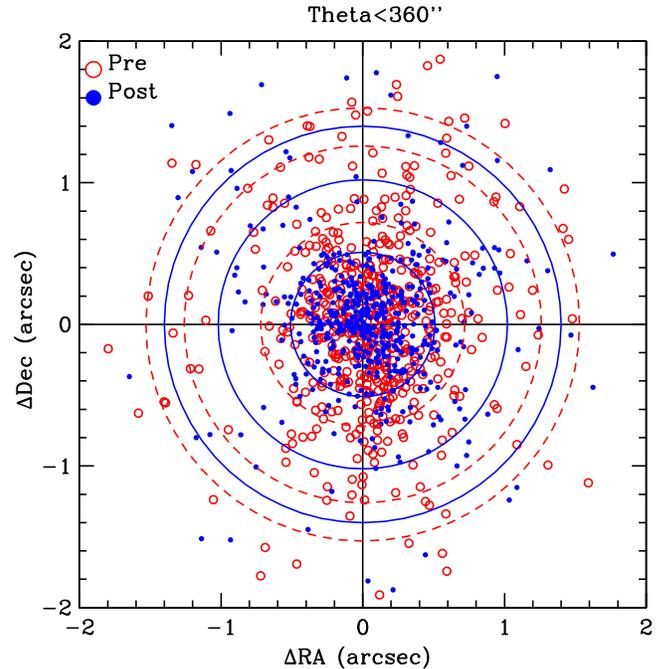


Figure 3. X-ray to I-band separation ($\Delta R.A.$, $\Delta Decl.$) in arcseconds for X-ray sources within $6'$ from the aim point detected in each single observation before (red open circles) and after (blue solid circles) the aspect correction. The circles encompass 68%, 90%, and 95% of the sources before (red dashed line) and after (blue solid line) the correction.

The background maps were computed for each observation separately in the full, soft, and hard bands. We ran `WAVDETECT` with a threshold parameter of $sigthresh = 10^{-5}$ corresponding to ~ 100 spurious sources per field (see Section 3.1), which was large enough to also select sources with significant signals only in stacked emission. We then removed these sources from the science images by excising a region corresponding to the source size (using a 3σ value) as computed by the detection tool. We then uniformly distributed the remaining counts and rescaled by the ratio between the whole area of the observation and the area without the removed sources. These files were then used as initial background.

We then downloaded “stowed background” data from the *Chandra* archive.³⁴ Stowed background files are particle-only background files and are obtained when the ACIS detector is out of the focal plane. These files were then rescaled using the procedure described in Hickox & Markevitch (2006): we measured the ratio between the number of counts in our initial background (C_{data}) and in the stowed image (C_{stow}) in the

³⁴ <http://cxc.harvard.edu/ciao/threads/acisbackground/>

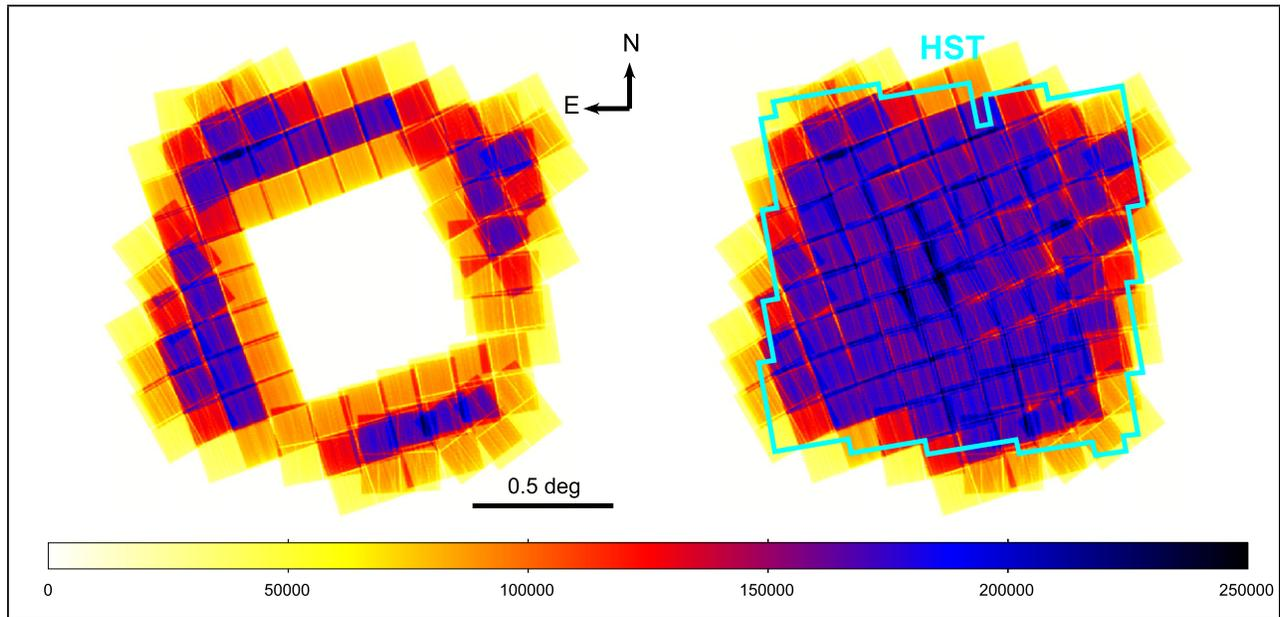


Figure 4. Mosaic of exposure maps for the new observations (left) and for the whole *COSMOS-Legacy* survey (right) in the full band. The color bar gives the achieved effective exposure in units of seconds. We reached a uniform coverage of ~ 160 ks over the full *HST* area (cyan polygon).

energy range 9.5–12 keV. In this band the effective area of *Chandra* is $\simeq 0$ and consequently all the counts have a non-astrophysical origin.

The stowed background was rescaled to our data by $C_{\text{data}}/C_{\text{stow}}$ and then subtracted from the initial background to obtain a first version of the cosmic X-ray background. The counts of this map were then renormalized using the exposure maps to create an exposure-corrected cosmic background.

Finally we performed a Monte Carlo simulation using the exposure-corrected cosmic X-ray background and the stowed background as input files. We simulated 1000 images for each of the two backgrounds using the IDL routine *poidev* to obtain a Poissonian realization of each map, and then we obtained our final homogeneous background map adding together the two mean simulated images. To use these maps for sensitivity computations and in our detection algorithm, a Gaussian smoothing (with a scale of 20 pixels) was applied to this final background map using the FTOOL *f_gauss*.

The distribution of the computed background (in counts arcsec^{-2}) in the three bands is reported in Figure 6. The overall background count distribution is consistent with the one found in C-COSMOS (see Figure 4 of P09). In the full band the main peak is at around 0.13 counts arcsec^{-2} and this corresponds to the deepest part of the exposure. In C-COSMOS the deep and shallow areas were roughly the same size and therefore the background distribution had two clear peaks of approximately the same height, while in *COSMOS-Legacy* the area with higher exposure is three times larger than the shallow area. This is represented in the background distribution as well. The number of background counts is consistent with the expectation for *Chandra* given the distribution of our exposure times.

4. DATA ANALYSIS: SOURCE DETECTION AND PHOTOMETRY

The analysis that follows focuses only on point sources. A parallel effort on the detection of extended sources will be

presented by A. Finoguenov et al. (2016, in preparation). To avoid contamination by extended sources we used the XMM-COSMOS catalog of extended sources (Finoguenov et al. 2007; Kettula et al. 2013) and visually inspected all the brightest ($L_X > 10^{41}$ erg s^{-1} in 0.5–2 keV) ones to check if a point source is detected inside them by *Chandra*.

Puccetti et al. (2009) extensively discussed and compared different source detection techniques and concluded that the best procedure for C-COSMOS was a combination of PWDetect (Damiani et al. 1997) and the *Chandra* Emldetect (CMLDetect) maximum likelihood algorithm. As shown by P09 using extensive simulations, one of the strongest features of PWDetect is its ability to locate X-ray sources with extreme accuracy ($0''.02 \pm 0''.15$, P09, Table 1) while CMLDetect is the best tool with which to perform source photometry and derive source significance. The *COSMOS-Legacy* survey shares the same tiling layout, exposure time per field, and roll angle range of C-COSMOS hence we can follow the P09 procedure and use the same significance threshold for source detection.

The original version of CMLDetect, called *emldetect* (Crudace et al. 1988; Hasinger et al. 1993), is part of the *XMM-Newton* SAS package and is based on a code originally developed for *ROSAT* data. CMLDetect has been adapted to run on *Chandra* data by replacing the *XMM-Newton* PSF library with the *Chandra* one (see Krumpel et al. 2015 for another application of CMLDetect). Moreover, this new tool can also work with different PSFs simultaneously.

PWDetect was developed to properly treat *Chandra* data with PSF varying across the field and it is based on the wavelet transform (WT) of the X-ray image. A WT is the convolution of an image with a “generating wavelet” kernel which depends on position and length scale (a free parameter). For this survey and for *Chandra* data in general, the length scale varies from $0''.5$ to $16''$ in steps of $\sqrt{2}$. These steps cover all possible *Chandra* PSFs (the largest are those at large off-axis angle θ_i). Both radial and azimuthal PSF variations are accounted for by

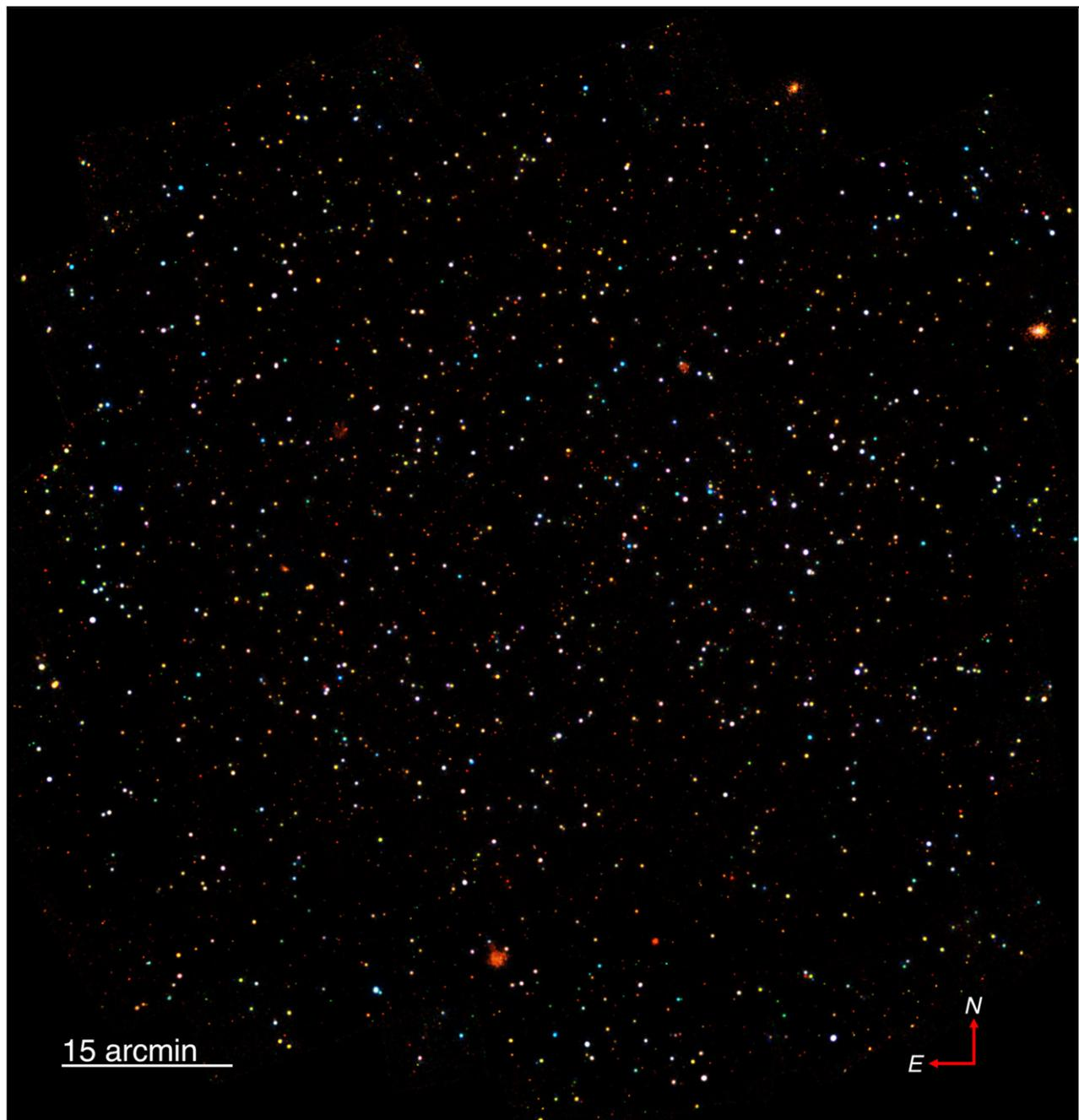


Figure 5. Three-colored image of the whole *COSMOS-Legacy* field (0.5–2.0 keV, 2.0–4.5 keV, and 4.5–7.0 keV as red, green, and blue, respectively).

`PWDetect` which first assumes a Gaussian PSF and then corrects by a PSF shape factor, calibrated with respect to source positions on the CCD.

`PWDetect` works on stacked observations only if coaligned (same aim point and roll angle) as is the case for 11 of our fields which are observations split into multiple parts. Therefore, `PWDetect` was run on each of our new 56 fields setting the detection limit to 3.8σ and corresponding to a probability of a spurious detection to $\simeq 10^{-4}$ with the aim of creating a large catalog of detections to be fed to `CMLDetect`. Also, given that the outer frame of C-COSMOS overlaps with the new survey, we run `PWDetect` on 20 old fields (fields 1–1 to 1–6, 1–6 to 6–6, 6–6 to 6–1, and last, 6–1 to 1–1 as in Table 3 of E09). For overlapping regions between different pointings we performed

a positional cross-correlation (using a $2''$ radius) and if a source was detected in more than one field we chose the position of the source at the smallest θ_i , i.e., the one with the best PSF. We performed a visual inspection of all the sources having multiple matches within $5''$. About 90% of the pairs in the range $2''$ – $5''$ were actually false detections, mainly caused by PSF tail detection of bright sources.

The positions obtained with `PWDetect` were then fed as input to `CMLDetect` to obtain photometric information and significance for each source. We ran `CMLDetect` allowing the detection only of point-like sources. `PWDetect` can be used to obtain net counts, rates, and fluxes, but we opted to use `CMLDetect` because it can work on a mosaic while `PWDetect` cannot. Moreover, P09 has shown that `PWDetect`

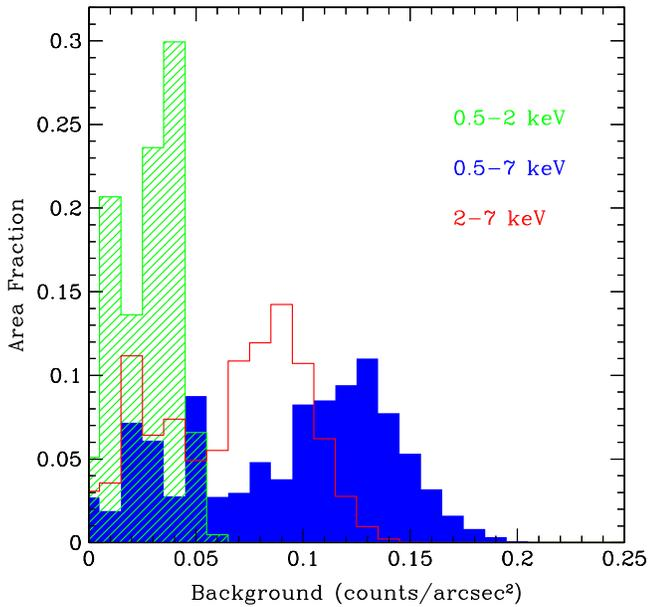


Figure 6. Distributions of background counts per square arcsecond in the full (solid blue histogram), soft (shaded green histogram), and hard (empty red histogram) bands.

count rates are systematically less accurate than those of CMLDetect (the median ratio between the output detected and input simulated count rates ranges from 86% to 94% for PWDetect versus 97% to 105% for CMLDetect, independently from the energy). CMLDetect performs a simultaneous maximum likelihood PSF fitting for each input candidate source, previously obtained using PWDetect, to all images at each position and working on a mosaic can provide a refined position of the source and count rates. This procedure was run in three bands: full (0.5–7 keV), soft (0.5–2 keV), and hard (2–7 keV). With the goal of not missing close pairs, we run CMLDetect allowing to slightly change the input position provided by PWDetect.

The best-fit maximum likelihood parameter in CMLDetect, DET_ML , is related to the Poisson probability that a source candidate is a random fluctuation of the background (P_{random}), as follows:

$$DET_ML = -\ln(P_{\text{random}}). \quad (1)$$

As a consequence, sources with small values of DET_ML have high values of P_{random} and are then likely to be background fluctuations. We chose a threshold significance value of 2×10^{-5} that corresponds to $DET_ML = 10.8$, i.e., a source needs to have $DET_ML > 10.8$ in at least one of the three bands to be included in the final catalog. This value is the same used in C-COSMOS and represents the best compromise between completeness and reliability as shown by P09 in Figures 11 and 12. Seventy-five percent of the sources detected by PWDetect in a single field with $DET_ML > 10.8$ and fed to CMLDetect were found to be above the threshold in output.

To improve the final completeness of the catalog we also search for less significant sources up to about 100 times higher P , which corresponds to a threshold $DET_ML = 6$. Similar to what was done in C-COSMOS, sources with DET_ML in the range 6–10.8 are only considered in this catalog if these have $DET_ML > 10.8$ in another band. Sources with $DET_ML < 6$ are considered undetected.

Table 2

Number of Sources with $DET_ML > 10.8$ in at Least one Band, for each Combination of X-Ray Bands

Bands	New	C-COSMOS	Legacy
F+S+H	1140	1047 (922)	2187
F+S	536	397 (474)	933
F+H	448	231 (257)	679
F	121	49 (73)	170
S	21	17 (32)	38
H	7	2 (3)	9
Total	2273	1743 (1761)	4016

Note. The “New” column includes all the newly detected sources. The columns labeled as “C-COSMOS” include the updated numbers using the information from the new data. The old numbers reported in parentheses are as in Elvis et al. (2009).

P09 performed extensive Monte Carlo simulations for C-COSMOS to both test the detection and photometry strategy as well as to determine the completeness and reliability of the source catalog at the chosen DET_ML threshold. Given that *COSMOS-Legacy* is the scaled-up version of C-COSMOS (in area and exposure), the same analysis was followed; hence, we infer that the completeness and reliability of the catalog are the same. Therefore, the chosen DET_ML threshold implies a completeness of 87.5% and 68% for sources with at least 12 and 7 full-band counts, of 98.2% and 83% for the soft band, 86% and 67% for the hard band. At this significance level and the same count limits the reliability is $\sim 99.7\%$ for the three bands.

4.1. Point Source Catalog

4.1.1. Source Numbers

We positionally matched the three single-band CMLDetect output catalogs (including all the sources to $DET_ML = 6$) to one another using a cross-correlation radius of $3''$. We first matched the full-band detected source catalog to the soft-band one then the full- with the hard-band catalog and finally the soft and hard-band one. We performed a visual inspection of the whole sample and also made use of the catalog of optical/IR identifications (presented in a companion paper, Marchesi et al. 2016) to solve ambiguous cases. After the visual inspection we found that $< 1\%$ of the matches were actually fake associations and all related to sources at the outer edges of the survey with rather wide PSFs and therefore with large positional error. Overall the mean (median) separation between detections of the same source in two different bands is $0''.43$ ($0''.23$) for full to soft and $0''.41$ ($0''.23$) for full to hard with 90% of the matches within $1''$. For soft to hard matches the mean (median) separation is instead $0''.73$ ($0''.56$), with $\sim 80\%$ within $1''$. The source position is determined in the full band for all the sources detected in the full band; if a source is not detected the full band, the soft band position is used. The hard band position is used for sources detected in the hard band only.

In Table 2 we report the total number of new sources for each combination of bands while in Table 4 we report the number of sources detected in each band at the two adopted thresholds ($DET_ML > 10.8$ and $6 < DET_ML < 10.8$). The number of detections with $DET_ML > 10.8$ in at least one of three X-ray bands is 2273. The number of expected spurious

Table 3

Number of Spurious Sources with DET_ML > 10.8 with at Least 12 and 7 Full-Band Counts, Corresponding to a Reliability of 99.7% for the New Data, the Old C-COSMOS Data (as in P09, Section 5) and the Whole *COSMOS-Legacy*

Bands	New		C-COSMOS		Legacy	
	>7	>12	>7	>12	>7	>12
F	5	5	6	6	12	11
S	4	3	4	3	9	7
H	3	3	4	3	8	7

sources with DET_ML > 10.8 is reported in each band for two count limits in Table 3.

In the area where the new data overlap with the outer C-COSMOS frame, the exposure time is now double the previous mean exposure time (142 ks versus 72 ks) and 385 new sources are detected in addition to the 694 sources already in E09. For the last 694 sources with doubled exposure time, 676 have been detected in the new data as well. The 18 C-COSMOS sources not detected in the new data had DET_ML values in E09 in the three bands close to the threshold (DET_ML < 15); moreover, 10 of them were detected only in two out of three bands in E09 and the remaining eight were detected only in one band.

In Table 2 we include the number of sources in each combination of bands for the C-COSMOS area including the new data and also in parentheses the number of sources as in E09. The same old and new numbers are included in Table 4. In this paper we provide also an updated catalog of the C-COSMOS sources with larger exposure in the total data. Among the 676 C-COSMOS sources with new data only ~1.5%, ~2%, and ~3% in the full, soft, and hard band, respectively, have a DET_ML value which is below the threshold in the combined data while it was above the 10.8 DET_ML threshold in the C-COSMOS catalog, confirming the reliability of the detection method and the consistency between the analysis performed in E09 and P09 and the one performed here. The actual fraction of sources with DET_ML lower in the combined data set than in C-COSMOS is 14% in the full and 10% in the soft and hard bands. On average, sources with lower DET_ML in the new data set are in an area of the field where the ratio (exp_new - exp_old)/exp_old is 40% lower than the average ratio of the sources in the catalog. Therefore, the discrepancy could be explained with source variability.

The total number of sources summing the two data sets is reported in the last column of Table 2. Adding the new observations we more than double the sample with respect to C-COSMOS and obtain a catalog of 4016 sources, the largest sample of X-ray sources homogeneously detected and having uniform multiwavelength data (see Section 7 for a discussion and Marchesi et al. 2016). In comparison, other contiguous surveys with similar area in the literature have about 20% fewer sources than *COSMOS-Legacy* (see 3362 sources in Stripe 82 by LaMassa et al. 2013a, 2013b, 2015; 3293 in X-Bootes by Murray et al. 2005; 2976 in XDEEP2 by Goulding et al. 2012).

In Figure 7 we show the signal-to-noise ratio (S/N = count rate/count rate error) as a function of the DET_ML for the new sources with DET_ML > 10.8. In excellent agreement with the finding in C-COSMOS, the S/N increases smoothly with increasing DET_ML with a dispersion of a factor of 2 at both low and high DET_ML values.

4.1.2. Source Positional Errors

To compute the positional errors associated with the X-ray centroids given in the catalog ($\sqrt{\sigma_{R.A.}^2 + \sigma_{decl.}^2}$), we followed the prescription of P09 defining $err_pos = r_{PSF}/\sqrt{S}$, where S is the number of net (i.e., background subtracted) source counts in the full band in a circular region of radius r_{PSF} containing 50% of the encircled energy in the observation where the source is at the smallest off-axis angle. The positional errors are generally in very good agreement with those resulting from *CMLDetect*. In Figure 8 the positional error distribution is presented for all the new sources (black solid line), the old C-COSMOS sources (red dashed line), and the updated C-COSMOS distribution (blue dotted line). The sources plotted in the lowest bin are those with positional error values actually smaller than 0".1 which we set to 0".1, consistent with the work done in P09. These sources with small positional errors are just very bright objects (with ~240 mean full band counts; see next section).

The peak of the new sources distribution is ~0".6 and 85% of the sources have a positional error < 1". while C-COSMOS source distributions peak at around 0".4. This difference (the somewhat larger positional errors for the sources detected with the new data than for those detected in C-COSMOS) is due to the fact that as shown in Figure 9 the net counts distribution for the sources in the new data peaks at a lower value than for the C-COSMOS sources (therefore giving a smaller denominator in the formula of the positional error).

4.1.3. Source Counts and Fluxes

The count rates in three bands reported here were obtained with *CMLDetect*. Vignetting and quantum efficiency were taken into account when measuring the effective exposure time. The count rate error at 68% confidence level was computed using the equation $err_rate = \frac{\sqrt{C_S \cdot 90\% + (1+a) \times B_{90\%}}}{0.9 \times T}$, where C_S is the source net count estimated by aperture photometry using an extraction radius including 90% of the EEF for each observation where the source was detected; B is the background count estimated in the same aperture on the background maps used in *CMLDetect* and corrected with a factor $a = 0.5$ introduced to account for the uncertainties on the background estimation in a given position (see P09); T is the vignetting corrected exposure time.

In Figure 9 the net count distributions for the new sources in three bands are compared with those in E09 (C-COSMOS old) and also with the updated counts distribution of C-COSMOS (C-COSMOS new). The total is the sum of the new detections plus the updated C-COSMOS. The median (mean) value of net counts in the whole data set in full, soft, and hard bands is 30, 20, and 22 (80, 60, and 43), respectively, compared to C-COSMOS where we had 33, 22, and 23 (88, 65, and 46). The total number of net counts for the 676 C-COSMOS sources also detected in the new data set is on average 60%–80% larger than the number of counts in C-COSMOS only. As a consequence the updated C-COSMOS count histograms in Figure 9 are all shifted to a higher numbers of counts. While in the full band the peak of the distribution is still around 30 counts we more than double the number of sources with more than 70 full-band counts, for which it is possible to perform individual X-ray spectral analysis from 390 (Lanzuisi et al. 2013) to ~950 sources in *COSMOS-Legacy*.

The fluxes were obtained from the count rates using the relation $F = R \times (CF \times 10^{-11})$, where R is the count rate in

Table 4
Number of Sources Detected in each Band at the two Adopted Thresholds

Band	DET_ML ≥ 10.8			6 < DET_ML < 10.8		
	New	C-COSMOS	Legacy	New	C-COSMOS	Legacy
Full (F)	2146	1667 (1655)	3813	99	57 (71)	156
Soft (S)	1538	1382 (1340)	2920	159	79 (88)	238
Hard (H)	1325	1115 (1017)	2440	271	165 (165)	436

Note. The columns labeled as C-COSMOS include the updated numbers using the information from the new data. The old numbers are in parentheses as in Elvis et al. (2009).

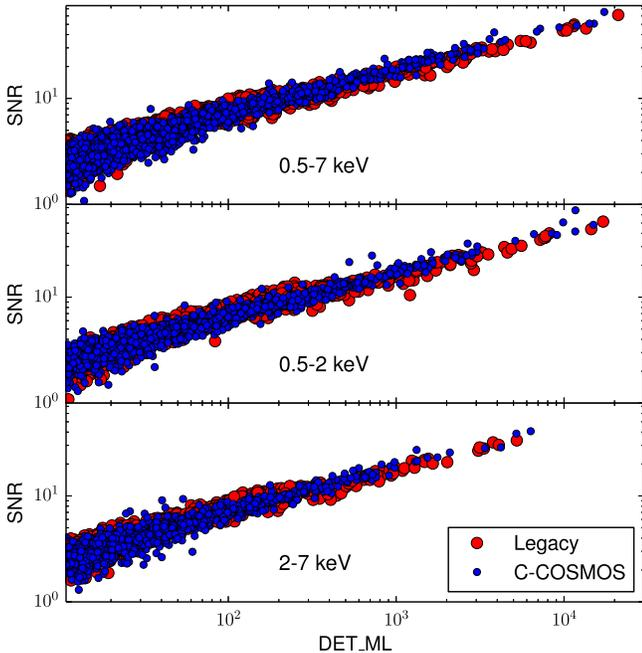


Figure 7. Signal-to-noise ratio as a function of DETML for sources detected in three bands. The new *Chandra* sources are plotted as red circles and the C-COSMOS sources as blue ones. We plot only sources with DETML > 10.8.

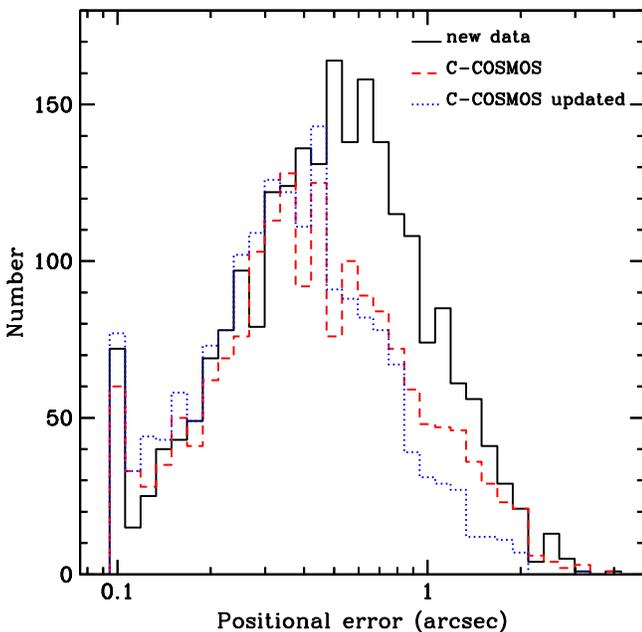


Figure 8. Positional error distribution for the new *COSMOS-Legacy* data (black solid line), the original C-COSMOS (red dashed line), and the updated C-COSMOS (blue dotted line).

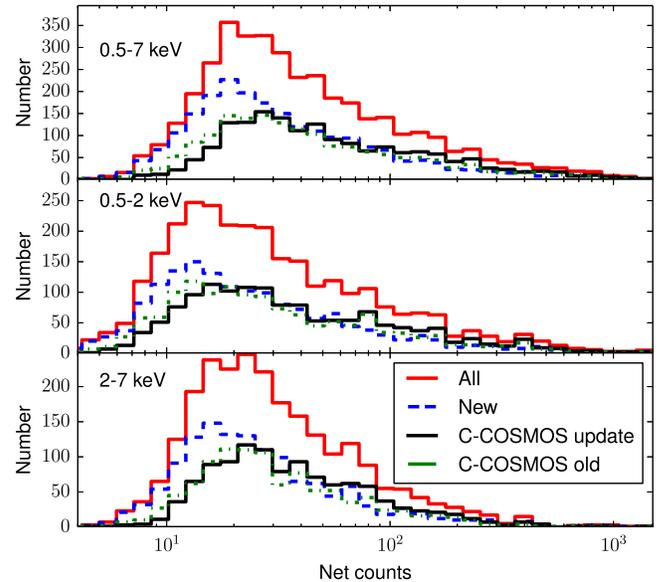


Figure 9. Source count distributions in three bands: 0.5–7 keV (top), 0.5–2 keV (center), and 2–7 keV (bottom) for *COSMOS-Legacy* (solid red line), new data only (blue dashed line), C-COSMOS old (green dotted-dashed), and updated (black solid). Sources with an upper limit have not been included.

each band and CF is the energy conversion factor computed using the CIAO tool *srcflux*, assuming a power-law spectrum with slope of $\Gamma = 1.4$ and a Galactic column density of $N_H = 2.6 \times 10^{20} \text{ cm}^{-2}$. Due to the fact that the observations have been taken in two different *Chandra* cycles, i.e., Cycle 8 for C-COSMOS and Cycle 14 for the new data, we used as CF a weighted mean of the factors in the different cycles depending on the exposure time for each source accumulated in each cycle to account for its variation ($\sim 15\%$ between the two cycles). The Cycle 14 (Cycle 8³⁵) CFs are 1.71 (1.57), 7.40 (6.34), and 3.06 (3.04) counts $\text{erg}^{-1} \text{ cm}^2$ for 0.5–10, 0.5–2, and 2–10 bands, respectively. The conversion factors are sensitive to the assumed spectral shape: for $\Gamma = 2$, there is a change of 40% in the full band CF, $\sim 5\%$ in the soft band and $\sim 20\%$ in the hard band.

For the 676 C-COSMOS sources detected in the new data as well, we computed new total X-ray fluxes. In Figure 10 the normalized distribution of ratios between total and old fluxes are plotted for the three bands. From Gaussian fitting of the distributions we find centroids at $(F_{\text{new}}/F_{\text{old}}) = 1.06, 1.11, 0.99$, and standard deviations of $\sim 0.50, \sim 0.55, \text{ and } \sim 0.40$ in

³⁵ The CF used for C-COSMOS and reported in E09 and P09 (computed using the online tool PIMMS) slightly differ from the one used here because the latter are now computed with the most updated response matrix. The difference is $\sim 15\%$ and it reflects on the final fluxes for all C-COSMOS sources.

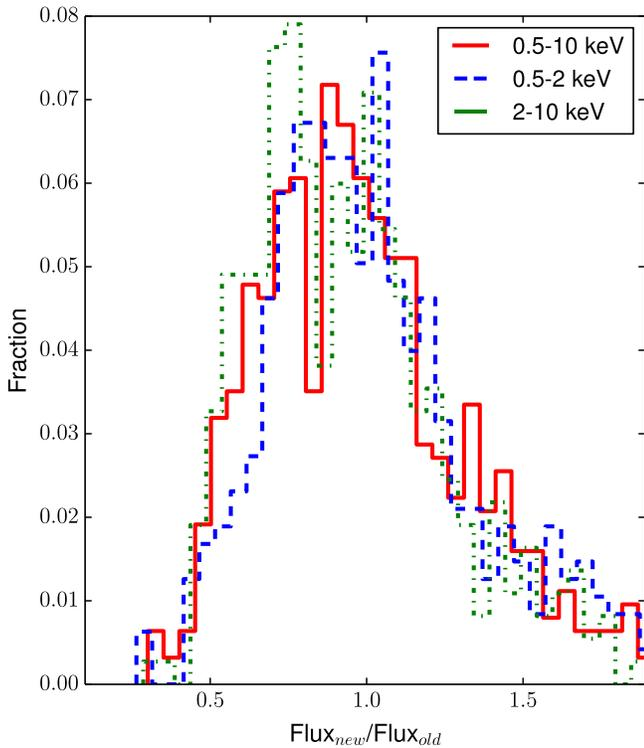


Figure 10. Normalized distributions of ratios between new and old fluxes of the 676 sources detected in C-COSMOS and also in the new data at DET_ML > 10.8. Sources with an upper limit have not been included.

full, soft, and hard bands, respectively, showing a good agreement between old and new fluxes. The distributions show wings to both negative and positive values. Malmquist bias is most likely responsible for the negative wing while variability for the positive one.

The distributions of X-ray fluxes for the whole *Chandra* COSMOS-Legacy survey in the full, soft, and hard bands is shown in Figure 11 where it is also compared with C-COSMOS (the new version with just the updated fluxes, given the excellent agreement) and XMM-COSMOS. The new survey is about ~ 2.5 times deeper than XMM-COSMOS in the 0.5–2 keV band and ~ 2 times in the 2–10 keV band and more than doubles the number of C-COSMOS sources in the same flux range. In the same figure we compare our data with the 4 Ms CDFS (Xue et al. 2011) and the large area Stripe 82 survey (LaMassa et al. 2013a, 2013b) source flux distributions, respectively to the left and to the right of *COSMOS-Legacy* flux distribution. The combination of the three surveys (the deepest, the intermediate, and among the widest; see also Section 7) allows to cover more than four orders of magnitude in flux.

Upper limits (90% confidence level) on net counts, count rates, and fluxes are given for all sources found in one band but not detected in another band. The upper limits were computed with the same procedure adopted for C-COSMOS and largely described in P09 to which we refer for a complete description.

4.1.4. Hardness Ratio (HR) Analysis

To provide a rough estimate of the X-ray spectral shape of the sources, in particular of the intrinsic obscuration (see Marchesi et al. 2016), for all the sources in the catalog including the C-COSMOS sources we computed the hardness ratio defined as $HR = \frac{H-S}{H+S}$, where H is the net count in the

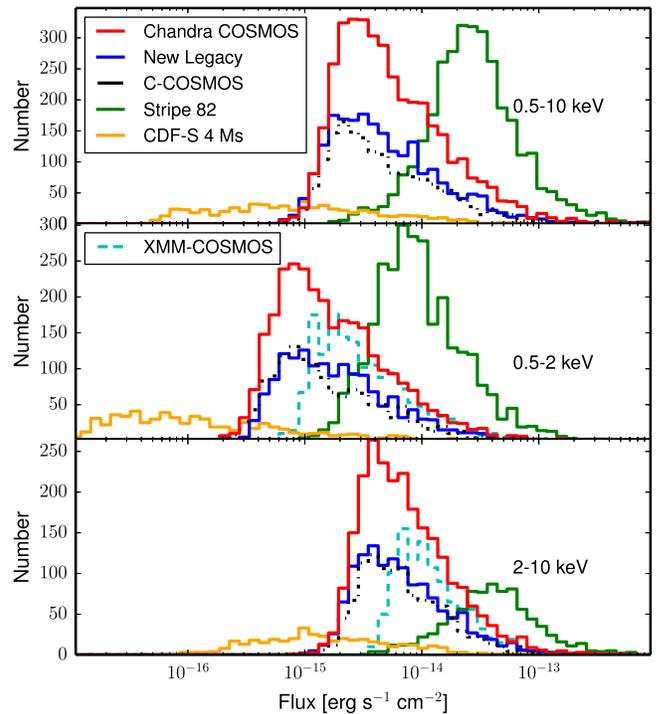


Figure 11. Flux distributions for sources detected in 0.5–10 keV (top), 0.5–2 keV (center), and 2–10 keV (bottom) bands for *COSMOS-Legacy* (solid red line), new data only (solid blue line), C-COSMOS updated (black dotted line) and XMM-COSMOS (cyan dashed line) sources. We also include the CDFS 4 Ms source flux distribution (orange line) and the Stripe 82 sources (green line). Sources with an upper limit have not been included.

hard band and S is those obtained in the soft band. Given the low number of counts for most of the sources (see Figure 9), we used BEHR (Bayesian Estimation of HRs, Park et al. 2006) which is particularly effective in the low-count regime, not needing a detection in both bands to work.

We extracted aperture photometry counts from each observation where the source was detected using the PSF radius at $EEF = 0.9$. We also extracted the background counts from the same observations using an annulus with $r_{\min} = r_{\text{PSF}} + 8$ pixels and $r_{\max} = r_{\text{PSF}} + 40$ pixels, where r_{PSF} is the PSF radius at $EEF = 0.95$ (in pixels). In the background extraction we excluded the contamination by other nearby detected sources using an exclusion radius equal to r_{PSF} . Total counts, background counts, and the ratio between the sum of background areas and the sum of source areas, both in soft and hard bands, were then fed as input parameters to BEHR.

For most sources (>3000) BEHR finds a detection on the HR and for 989 sources an upper or lower limit (616 and 371 sources, respectively). The typical error on the HR is ~ 0.2 . In Figure 12 we plot the distribution of the HRs for the measured values (black solid line), for the lower limits (red solid line) and the upper limits (blue solid line). The mean (median) HR value is -0.09 (-0.17) for the measured values and it moves to lower values when including upper and lower limits (-0.11 and -0.19 for the mean and the median, respectively). A Gaussian fit returns a peak at -0.20 with a 1σ dispersion of 0.32; however, a single Gaussian is not clearly a best representation of the HR distribution. A double Gaussian fit returns a peak at -0.31 and one at 0.12 with a 1σ dispersion of 0.18 and 0.38, respectively.

HR is not a fully reliable measurement of obscuration because of the complexity of the spectral shape, the large error

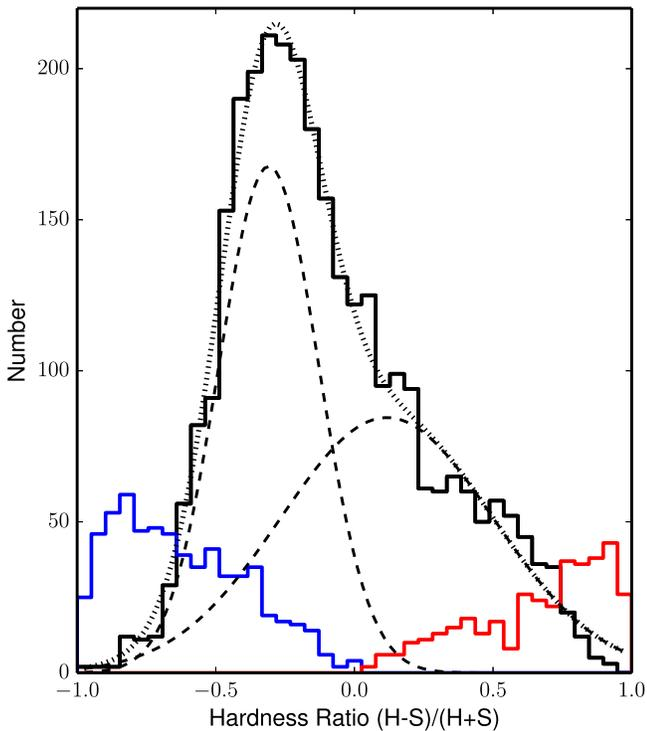


Figure 12. HR distributions for the whole sample (black solid line), upper limits (blue solid line) and lower limits (red solid line). The dotted line is the sum of the double Gaussian fitting. The dashed lines are the two Gaussian resulting from the fitting.

bars due to low counts statistic, and the redshift dependency (see Marchesi et al. 2016); however, it is possible to roughly assume an HR value to divide the sources in obscured and unobscured. We use here $HR = -0.2$ which has been shown to be a fair value to separate sources with column densities above and below 10^{22} cm^{-2} (Civano et al. 2012; Lanzuisi et al. 2013) at all redshifts. A total of 1993 sources, $50^{+17}_{-16}\%$ of the entire sample (errors have been computed using HR 1σ errors) are therefore classified as obscured. Tentatively the double Gaussian fit of the HR distribution could also be interpreted as to be due from two populations of sources, the obscured population peaking at positive HRs and the unobscured population peaking at negative HR. The broad dispersion of the Gaussian peaking at positive HR could be due to high redshift-obscured sources whose HR would be negative even if obscured. A more detailed analysis on the obscured AGN fraction is presented in Marchesi et al. (2016).

4.1.5. Source Catalog

The catalog released with this paper contains all the measurements discussed above. In Table 5 we show the columns of the catalog of the new 2273 sources (named as “lid” in column 1) combined with the updated C-COSMOS catalog of 1743 sources (named as “cid” in column 1). The catalog will also be stored on the COSMOS website at the *COSMOS-Legacy* project page.³⁶ Data products including exposure and events mosaics are available in the dedicated page³⁷ at the same website.

³⁶ <http://irsa.ipac.caltech.edu/data/COSMOS/tables/chandra/>

³⁷ <http://irsa.ipac.caltech.edu/data/COSMOS/images/chandra/>

Table 5
Data Fields in the Catalog

No.	Field	Note
1	Name	<i>Chandra</i> source name
2	R.A.	<i>Chandra</i> Right Ascension (J2000, hms)
3	Decl.	<i>Chandra</i> Declination (J2000, dms)
4	pos_err	Positional error (arcsec)
5	DET_ML_F	maximum likelihood detection value in 0.5–7 keV band
6	rate_F	0.5–7 keV count rate (counts s^{-1})
7	rate_F_err	0.5–7 keV count rate error (counts s^{-1})
8	flux_F	0.5–10 keV flux (erg $\text{cm}^{-2} \text{s}^{-1}$)
9	flux_F_err	0.5–10 keV flux error (erg $\text{cm}^{-2} \text{s}^{-1}$)
10	snr_F	0.5–7 keV S/N
11	exptime_F	0.5–7 keV exposure time (ks)
12	cts_ap_F	0.5–7 aperture photometry counts (counts)
13	cts_ap_F_err	0.5–7 aperture photometry counts error (counts)
14	DET_ML_S	maximum likelihood detection value in 0.5–2 keV band
15	rate_S	0.5–2 keV count rate (counts s^{-1})
16	rate_S_err	0.5–2 keV count rate error (counts s^{-1})
17	flux_S	0.5–2 keV flux (erg $\text{cm}^{-2} \text{s}^{-1}$)
18	flux_S_err	0.5–2 keV flux error (erg $\text{cm}^{-2} \text{s}^{-1}$)
19	snr_S	0.5–2 keV S/N
20	exptime_S	0.5–2 keV exposure time (ks)
21	cts_ap_S	0.5–2 aperture photometry counts (counts)
22	cts_ap_S_err	0.5–2 aperture photometry counts error (counts)
23	DET_ML_H	maximum likelihood detection value in 2–7 keV band
24	rate_H	2–7 keV count rate (counts s^{-1})
25	rate_H_err	2–7 keV count rate error (counts s^{-1})
26	flux_H	2–10 keV flux (erg $\text{cm}^{-2} \text{s}^{-1}$)
27	flux_H_err	2–10 keV flux error (erg $\text{cm}^{-2} \text{s}^{-1}$)
28	snr_H	2–7 keV S/N
29	exptime_H	2–7 keV exposure time (ks)
30	cts_ap_H	2–7 aperture photometry counts (counts)
31	cts_ap_H_err	2–7 aperture photometry counts error (counts)
32	hr	Hardness ratio
33	hr_lo_lim	Hardness ratio 90% lower limit
34	hr_up_lim	Hardness ratio 90% upper limit

(This table is available in its entirety in machine-readable form.)

4.2. Matching with XMM-COSMOS Catalog

We matched the *COSMOS-Legacy* sources with those in XMM-COSMOS (Cappelluti et al. 2009). There are 1714 secure XMM-COSMOS sources with at least one counterpart in *COSMOS-Legacy*, 824 of which have at least one counterpart in the new data. There are 46 XMM-COSMOS sources outside the area covered by *COSMOS-Legacy* (see Figure 1) and 126 with no *Chandra* counterparts. In summary, 93% of the XMM-COSMOS sources within the *COSMOS-Legacy* area have at least one *Chandra* counterpart.

The 126 sources with no *Chandra* counterparts can be divided into three groups: the 25 sources (20%) with *Chandra* exposure ≥ 40 ks; the 60 sources (48%; 13 of these sources have also *Chandra* exposure < 40 ks) with XMM-COSMOS $DET_ML < 15$ in all of the three bands (0.5–2 keV, 2–8 keV, 4.5–8 keV); and last, the 54 sources with XMM-COSMOS $DET_ML > 15$ in at least one band and *Chandra* exposure > 40 ks. For the first group the low exposure time could be the reason for the non-detection while for the second

group the non-detection in *Chandra* can be explained with a flux fluctuation within the flux uncertainty. We visually inspected the sources in the last group and we found that seven of them are located inside a bright cluster and therefore have not been resolved into point sources by our analysis. For the remaining 47 sources the *Chandra* signal is weak or negligible and therefore these sources could be candidate variable AGN. In particular, XMM-ID 30748 has DET_ML 20 times larger than the detection threshold in XMM-COSMOS; this source was detected only in the 0.5–2 keV band, with a flux of $F = 2.7 \times 10^{-15} \text{ erg s}^{-1} \text{ cm}^{-2}$ and a photometric redshift of $z = 2.71$. Despite being interesting and worth further analysis on the variability, this is beyond the scope of this paper.

There are 58 XMM-COSMOS sources that have been resolved by the smaller *Chandra* PSF into two distinct sources using a maximum radius of $10''$ for the match. Two XMM-COSMOS sources have been resolved into three *Chandra* sources using a maximum radius of $10''$. As a comparison, 25 XMM-COSMOS sources (Brusa et al. 2010) were resolved into two separate C-COSMOS sources. More details on the optical counterparts of the XMM-COSMOS sources resolved in two *Chandra* ones are given in Marchesi et al. (2016).

There is a good agreement between XMM-COSMOS and *Chandra* fluxes. We rescaled the *Chandra* COSMOS-Legacy fluxes using the same slope used for XMM-COSMOS ($\Gamma = 2$ in soft band and $\Gamma = 1.7$ in hard band) and found that the median value of the ratio $\text{flux}_{\text{XMM}}/\text{flux}_{\text{Chandra}}$ is 1.13 in soft band and 1.22 in hard band.

5. SKY COVERAGE AND SURVEY SENSITIVITY

The sky coverage of a survey is the area covered as a function of the flux limit. We computed it in three bands (0.5–10, 0.5–2, and 2–10 keV) using the exposure and background maps (see Sections 3.2 and 3.3) produced for the source detection and assuming a power-law spectrum with $\Gamma = 1.4$ and Galactic $N_H = 2.6 \times 10^{20} \text{ cm}^{-2}$. X-ray observations have a flux limit that changes over the field of view because the *Chandra* PSF changes in both size and shape as a function of the distance from the aim point and because the effective area is vignettted. In this survey where the total coverage is obtained using multiple overlapping pointings, every source was observed in up to six different positions on the detector which resulted in a quite uniform average PSF (Figure 2).

The procedure we used to compute *COSMOS-Legacy* survey sky coverage is closely similar to that used by P09 for C-COSMOS but makes use of a PSF map for each observation instead of an analytical form of the PSF as function of the off-axis angle. This is a more time-consuming approach but one that returns a more detailed sensitivity map that can be valuable in other studies (e.g., clustering analysis and correlation functions) or simply for source photometry (Section 4.1.4).

For each observation we made use of the CIAO tools `mkpsfmap` and `dmimgadapt` to create a background map convolved with the PSF map in such a way that at each position of the map the count value corresponds to the number of counts in an aperture corresponding to 50% of the EEF at that position.

For each position of the entire mosaic (applying a binning of 8 pixels for computing time purposes) we computed the minimum number of counts C_{min} needed to exceed the

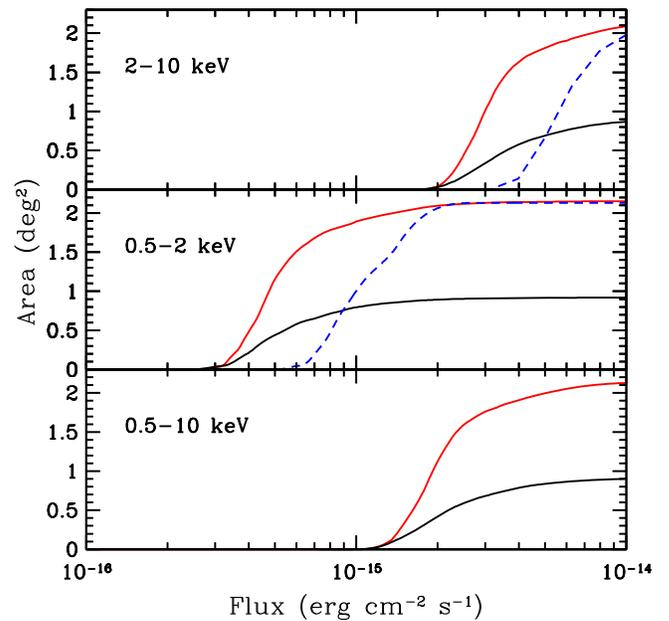


Figure 13. Area-flux curve for *COSMOS-Legacy* (red solid line) in 2–10 keV (top), 0.5–2 keV (center) and 0.5–10 keV (bottom) bands. The coverage of C-COSMOS (black solid line) and XMM-COSMOS in the 0.5–2 keV and 2–10 keV bands (Cappelluti et al. 2009; blue dashed line) are shown for comparison.

background fluctuations, assuming the same probability for spurious sources (i.e., DET_ML threshold) used in the C-COSMOS and *COSMOS-Legacy* catalogs for the Poisson statistics, i.e., 2×10^{-5} . We used the relation

$$P_{\text{Poisson}} = e^{-B} \sum_{k=C_{\text{min}}}^{\infty} \frac{B^k}{k!} = 2 \times 10^{-5}, \quad (2)$$

where B is the total background count computed at each position of the grid, by summing the background counts in each observation covering that given position. Equation (2) is solved iteratively to find C_{min} ; then the count rate limit, R_{lim} is obtained using

$$R_{\text{lim}} = \frac{C_{\text{min}} - B}{f_{\text{psf}} \times T_{\text{exp}}}, \quad (3)$$

where T_{exp} is the total vignetting corrected exposure time at each position on the grid, while f_{psf} is the encircled count fraction of the PSF. In C-COSMOS this value was tuned to reproduce the simulation results and then it was fixed to $f_{\text{psf}} = 0.5$. However, any number in the range 0.5–0.9 produced similar results with variations of the order of few percent in the resulting sensitivity.

Finally we converted the count rate limit R_{lim} into the flux limit using the same conversion factors used for the sources in the catalog based on the position (see Section 4.1.3). We also computed the sensitivity for only the C-COSMOS area with the same method and obtained the same sensitivity as published in E09 and P09.

The sky coverage of the *Chandra* COSMOS-Legacy survey in the three energy bands is shown in Figure 13. We compare our results with those of C-COSMOS (black solid lines) and XMM-COSMOS (blue dashed lines). The new survey covers a similar area to XMM-COSMOS and almost three times the area

of C-COSMOS at faint fluxes (e.g., $\sim 5 \times 10^{-15} \text{ erg cm}^{-2} \text{ s}^{-1}$ in the soft band) and ~ 2 times at bright fluxes (e.g., $> 10^{-15} \text{ erg cm}^{-2} \text{ s}^{-1}$ in the soft band).

We have verified that the limits at 20% (50%) completeness for the Legacy catalog are consistent with those computed and reported in Table 2 of P09 and assuming the changes in CF used here and explained in Section 4.1.3 of $1.5 (1.9) \times 10^{-15}$, $3.9 (4.9) \times 10^{-16}$ and $2.5 (3.1) \times 10^{-15} \text{ erg cm}^{-2} \text{ s}^{-1}$ in the F, S, and H bands. At this limit, *COSMOS-Legacy* increases by a factor of 3 the area covered with respect to C-COSMOS.

6. NUMBER COUNTS

The $\log N$ – $\log S$ relation, i.e., the number of sources $N(>S)$ per square degree detected at fluxes brighter than a given flux S ($\text{erg s}^{-1} \text{ cm}^{-2}$), provides a first estimate of source space density as a function of flux and therefore information on the cosmic population to compare with different models of population synthesis. Given that multiple $\log N$ – $\log S$ curves have been published in the literature, it is also a standard check to validate the many calibration steps used to produce a catalog of X-ray point-like sources.

We constructed the $\log N$ – $\log S$ curve for *COSMOS-Legacy* in both the 0.5–2 keV and 2–10 keV bands. Following P09 we included only sources with $\text{DET_ML} > 10.8$ and we applied a cut in S/N (> 2 and > 2.5 in soft and hard) to limit the Eddington bias effect, which could have a significant (up to 30%–50%) contribution at the lowest fluxes. This choice avoids sources with large statistical uncertainties on their fluxes and limits the errors due to the sky coverage uncertainties at the faint end. With the adopted thresholds in S/N the agreement measured in P09 between simulations input and output $\log N$ – $\log S$ is better than 5%. The procedure used by P09 is consistent with the one applied by Luo et al. (2008) on *Chandra* Deep Field South data. The number of sources not included because of the S/N cut is $\sim 1\%$ in the soft and $\sim 5\%$ in the hard band.

The adopted S/N s imply the following flux limits: $2.7 \times 10^{-16} \text{ erg s}^{-1} \text{ cm}^{-2}$ in the 0.5–2 keV band and $1.8 \times 10^{-15} \text{ erg s}^{-1} \text{ cm}^{-2}$ in the 2–10 keV band. These are the same flux limits of C-COSMOS, which is expected given that the new observations have the same maximum exposure. The final number of sources used here for the number counts with the above constraints are 2758 in the soft band (1309 from C-COSMOS and 1449 from the new sample) and 2243 in the hard band³⁸ (1056 from C-COSMOS and 1187 from the new sample).

We show the results obtained with these source selections in Figure 14. In the top panels the normalized Euclidean curves, i.e., with $N(>S)$ multiplied by $S^{1.5}$, are presented in order to enhance the differences between different surveys. In the same figure we include the C-COSMOS (E09) and XMM-COSMOS points (Cappelluti et al. 2009). We also compare our $\log N$ – $\log S$ relationships with those from previous X-ray surveys, spanning from wide (Stripe 82 XMM: LaMassa et al. 2013a; 2XMM: Mateos et al. 2008), to moderate (XDEEP2: Goulding et al. 2012) to small areas (4 Ms CDFS: Lehmer et al. 2012). As XDEEP2 and CDFS define their hard band in a slightly different energy range we converted their energy to 2–10 keV to perform an adequate comparison.

COSMOS-Legacy $\log N$ – $\log S$ covers 3 and 2.5 orders of magnitude in flux in the soft and hard band, respectively, with 2%–8% errors at fluxes $< 1\text{--}3 \times 10^{-14} \text{ erg cm}^{-2} \text{ s}^{-1}$, respectively. The excellent statistics allow considerable reduction in the uncertainties (20%–30%) in the number counts also at bright fluxes which are now $\simeq 40\%$ smaller than in C-COSMOS.

In the soft band there is an excellent agreement between our survey and previous works below $S \sim 10^{-14} \text{ erg cm}^{-2} \text{ s}^{-1}$. At brighter fluxes instead the uncertainties are larger due to the low number of detections (65 sources in *COSMOS-Legacy*). A larger spread is observed when comparing results from different surveys due to the fact that bright sources can be properly sampled only with extremely large areas ($> 5\text{--}10 \text{ deg}^2$). In the hard band instead, *COSMOS-Legacy* number counts agree with other surveys at faint fluxes while at the bright end (i.e., $S > 2 \times 10^{-14} \text{ erg cm}^{-2} \text{ s}^{-1}$) the *COSMOS-Legacy* counts are in the upper envelope of the spread.

We also compare our results with predictions of two different phenomenological models, Gilli et al. (2007) and Treister et al. (2009), assuming column densities in the interval $N_H = 10^{20\text{--}26} \text{ cm}^{-2}$ and redshift $z = 0\text{--}6$. In Figure 14 (bottom panels) we show the ratio of *COSMOS-Legacy* number counts to both models in the soft and hard bands (left and right). At the faint end of the soft band, i.e., up to fluxes $\sim 10^{-14} \text{ erg cm}^{-2} \text{ s}^{-1}$, our results are in agreement with the Gilli et al. (2007, solid points) model prediction within 1%–5% while the Treister et al. (2009, open points) model (open points) slightly underpredicts the counts by 5%–10% in the same flux range. At bright fluxes where the sample is limited by the statistics the differences between models and data becomes larger, even exceeding 10%. In the hard band both models reproduce well the observed data within 5% below $> 2 \times 10^{-14} \text{ erg cm}^{-2} \text{ s}^{-1}$ and the difference becomes more pronounced at bright fluxes ($> 10\%$ at fluxes $> 5 \times 10^{-14} \text{ erg cm}^{-2} \text{ s}^{-1}$).

The Gilli et al. (2007) and Treister et al. (2009) models are based on different assumptions on the fraction of obscured sources and on the assumed luminosity and redshift dependences. Therefore, their differences are more marked when considering obscured and unobscured sources separately. We used the HR as defined in Section 4.1.4 to divide the sample using $\text{HR} > -0.2$ for obscured sources and $\text{HR} < -0.2$ for unobscured sources. In the soft (hard) band there are 1057 (1332) obscured sources and 1701 (911) unobscured ones. In Figure 15 we present the number counts in the soft and hard bands (left and right) for both obscured (red) and unobscured (blue) sources. A clear difference is observed in the number counts of obscured and unobscured in the soft band where we observe a ratio of up to ~ 10 at bright fluxes while it almost disappears in the hard band, where the ratio is very small at all fluxes. This implies that the difference must be dictated by obscuration effects.

The models from Gilli et al. (2007, solid lines) and Treister et al. (2009, dashed lines), assuming column densities above and below 10^{22} cm^{-2} (red and blue, respectively), are plotted in the same Figure. In the soft band both predictions of the number of unobscured sources are in agreement within 5% with our data up to fluxes of $\sim 3 \times 10^{-14} \text{ erg cm}^{-2} \text{ s}^{-1}$ while the difference becomes larger for obscured sources ($> 10\%$ – 20%) with both models overpredicting the number of sources at all fluxes. In this last case the Treister et al. (2009) model predictions are generally worse than those of the Gilli et al. (2007) model by 5%–10%. In the hard band instead,

³⁸ We also applied a cut in exposure time at 40 ks in the hard band to limit sources (65 in total) at the edges of the field with high background level.

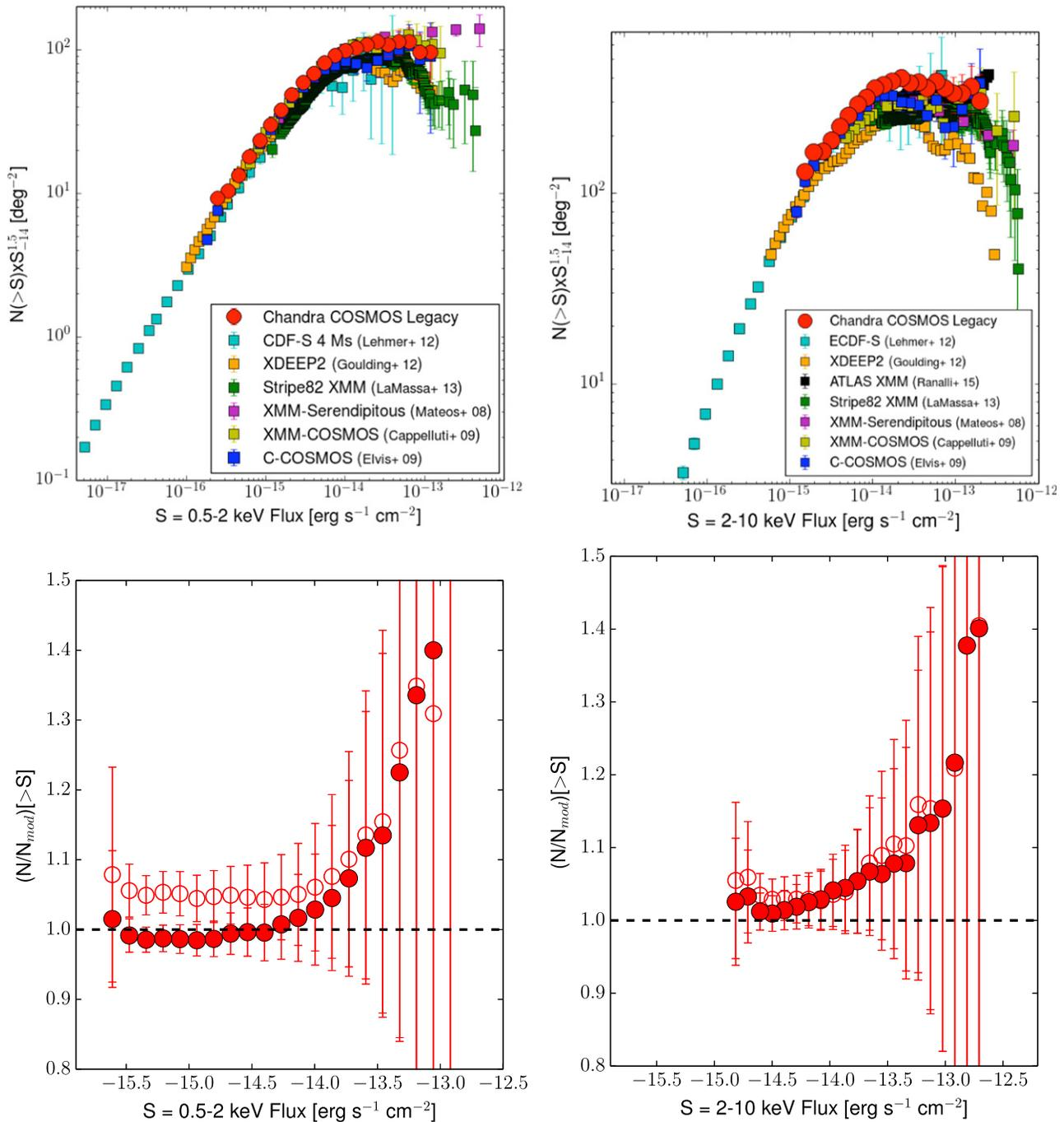


Figure 14. Euclidean normalized $\log N$ - $\log S$ curves in 0.5–2 keV (top left) and 2–10 keV (top right) bands. The *COSMOS-Legacy* curve for all sources with $\text{DET_ML} > 10.8$ and $S/N > S/N_{\text{lim}}$ is plotted in red circles. Results from previous works are plotted (see label in the plot). The ratio of *COSMOS-Legacy* number counts to Gilli et al. (2007, red solid circles) and Treister et al. (2009; red empty circles) models are plotted in the soft and hard bands (bottom left and bottom right). The source number counts are multiplied by $(S/10^{14})^{1.5}$ to highlight the deviations from the Euclidean behavior.

model predictions are in general excellent agreement with our data (differences $< 5\%$ up to fluxes of $5 \times 10^{-14} \text{ erg cm}^{-2} \text{ s}^{-1}$) for both samples above and below $\text{HR} = -0.2$.

Overall these discrepancies between data and models are totally expected given that, for example, a different spectral model could change source fluxes and sky coverage, and that the spectral parameters in the Gilli et al. and Treister et al. models are different from those used in this work. Therefore, despite all the underlying assumptions the differences between observed number counts and phenomenological models are remarkably small (2%–5%; see also LaMassa et al. 2013b for a

discussion on discrepancies between data and population synthesis models).

7. SUMMARY AND CONCLUSIONS

In this paper we presented *COSMOS-Legacy*, a 2.2 deg^2 *Chandra* survey of the COSMOS field. We employed a total of 4.6 Ms of exposure time including 1.8 Ms already published by E09 plus 2.8 Ms obtained as an X-ray Visionary Project during *Chandra* Cycle 14. The new data comprise 56 overlapping observations which, added to the 36 C-COSMOS

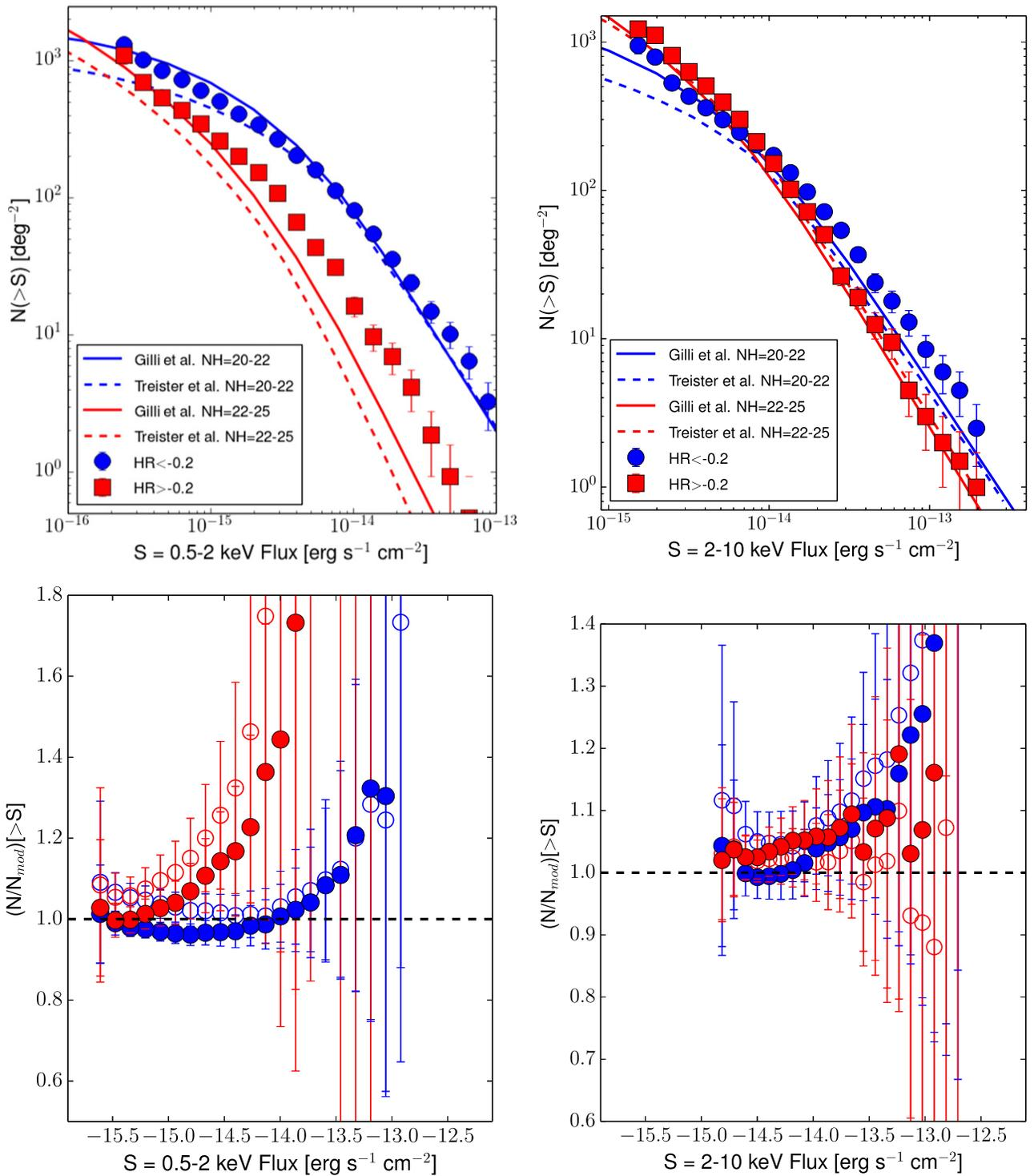


Figure 15. Number counts in soft (top left) and hard (top right) bands for sources with $HR > -0.2$ (red squares) and < -0.2 (blue circles) plotted with the Gilli et al. (solid lines) and Treister et al. (dashed lines) models with two different column density ranges $>10^{22} \text{ cm}^{-2}$ in red and $<10^{22} \text{ cm}^{-2}$ in blue. The ratio of *COSMOS-Legacy* number counts to Gilli et al. (2007; solid) and Treister et al. (2009; empty) models are plotted in the soft and hard bands (bottom left and bottom right).

pointings, yield a relatively uniform coverage of ~ 160 ks over the whole *Hubble*-covered area. By construction the survey flux limit is the same as C-COSMOS and computed in three bands using the same approach of P09.

We followed the same procedure used and tested by P09 combining standard CIAO tools for the data reduction and PWDetect and CMLDetect for the data analysis, including

the source detection and photometry. We also performed aperture photometry for consistency with the E09 and P09 analysis. The analysis was performed on the new *Chandra* data and also on the outer C-COSMOS frame, overlapping with the new observations. Given that the survey properties (exposure, roll angle, and background counts) are consistent with C-COSMOS ones, we used the same probability threshold

for the source detection corresponding to $\text{DET_ML} = 10.8$. At this limit we detected 2273 sources that were not previously detected in C-COSMOS, by combining detections in the full, soft and hard bands. In the area overlapping with C-COSMOS 385 of these sources were detected. In the same area we also found 676 of the 694 old detections while 18 sources were not detected again. The total number of sources in *COSMOS-Legacy* is 4016. The source properties including counts count rates, fluxes in three bands (full, soft, and hard), and HR were computed using a Bayesian approach and are reported in an online table published with this paper.

We computed the source number counts in both soft and hard bands and find good agreement between our results and other surveys in the literature as listed above. The large number of sources in *COSMOS-Legacy* (20% or more than the sources in other contiguous surveys) allow to constrain the number of counts at medium fluxes ($\sim 10^{-15}$ erg cm $^{-2}$ s $^{-1}$) with 10% errors and to reduce the uncertainties on the normalization at bright fluxes where discrepancies between different surveys still exist. The combination of *COSMOS-Legacy* with other surveys at fainter and brighter fluxes allows to cover more than 4 orders of magnitude in flux.

Using the HR we measure a fraction of obscured sources of $50_{-16}^{+17}\%$, defined as sources with $\text{HR} > -0.2$, that correspond to column density $> 10^{22}$ cm $^{-2}$ at all redshifts despite the uncertainties on the classification due to complex spectral modeling not taken into account in this work (see Wilkes et al. 2009, 2013). For the first time, we computed the number counts for obscured and unobscured sources separately using the HR as an indication for obscuration ($\text{HR} = -0.2$ corresponding to the separation between $>$ and $< 10^{22}$ cm $^{-2}$). The large number of sources in each sample (about 1000 or more) allowed us to compute the number counts for the two populations and revealed a larger difference (in both normalization and shape) in the soft band while a very small if not absent difference in the hard band was observed (the normalization is consistent while we can observe a small difference in shape). Given the large range of luminosities and redshifts probed by *COSMOS-Legacy* this can be interpreted as a difference in orientation rather than an intrinsic difference due to an evolutionary state between the obscured and unobscured sources.

In Figure 16 the area-flux parameter space of the most recent *Chandra* and *XMM-Newton* surveys (CDFS 4 Ms, Xue et al. 2011; AEGIS-XD, Nandra et al. 2015; XDEEP2-F1, Goulding et al. 2012; C-COSMOS, E09; XMM-COSMOS, Cappelluti et al. 2009; X-Bootes, Murray et al. 2005; XMM-Atlas, Ranalli et al. 2015; Stripe 82, LaMassa et al. 2013a, 2013b, 2015; XMM-XXL, PI: Pierre, see also Pierre et al. 2004) is presented. Most surveys lie on a locus (yellow shaded area) determined by our current X-ray telescope capabilities. *COSMOS-Legacy* is exploring a new region off this locus, which is an additional factor 2–3 deeper at the areas it covers, by using a total exposure time that is unusually large (4.6 Ms total) for that given area flux combination and is preparing for surveys with future facilities. The X-Bootes survey also explores a region off the survey locus but at brighter fluxes and over a larger area.

In future decades with facilities like *eROSITA* (Merloni et al. 2012), *Athena* (Nandra et al. 2013), and *X-ray Surveyor* (Vikhlinin et al. 2012), it will be possible to explore a new region of area-flux parameter space and move away from the

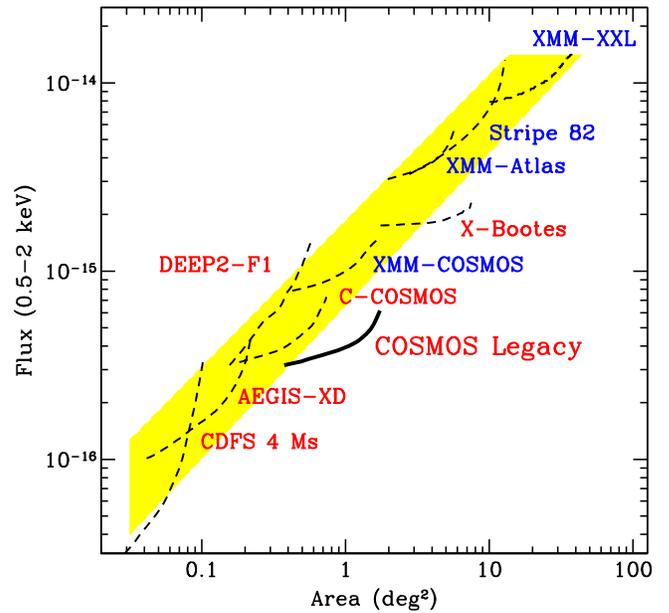


Figure 16. Area-flux curves for *Chandra* (red) and *XMM-Newton* (blue) contiguous X-ray surveys. Each survey has been plotted using each sensitivity curve starting from the flux corresponding to 80% of the maximum area for that survey to the flux corresponding to the 20% of the total area. The plotted surveys are CDFS 4 Ms (Xue et al. 2011), XDEEP2-F1 (Goulding et al. 2012), AEGIS-XD (Nandra et al. 2015), C-COSMOS (E09), XMM-COSMOS (Cappelluti et al. 2009), X-Bootes (Murray et al. 2005), XMM-Atlas (Ranalli et al. 2015), Stripe 82 (LaMassa et al. 2013a, 2013b, 2015), and XMM-XXL (PI: Pierre; see also Pierre et al. 2004). The survey locus described in the last section is drawn in yellow.

current survey locus toward the bottom right corner of Figure 16. For example, *Athena+* will perform a multi-tiered survey with a combination of a large effective area and field of view. This will enable X-ray surveys to be carried out two orders of magnitude faster than with *XMM-Newton* and *Chandra* (see Figure 2 of Aird et al. 2013). With a *Chandra*-like resolution over $10'$, *X-ray Surveyor* will be able to cover the same *COSMOS-Legacy* area at the same flux in only 55 ks (A. Vikhlinin 2015, private communication), 80 times faster than *Chandra*.

Thanks to the large area covered at considerable depth, *COSMOS-Legacy* can now address those questions for which a large number of detected X-ray sources at a medium depth with uniform multiwavelength coverage and almost complete redshift information is needed. The excellent positional accuracy allows us to obtain multiwavelength identifications and photometric redshifts for 96% of the sources (Marchesi et al. 2016). We are currently working on papers on the X-ray luminosity function with a focus on the high redshift universe (S. Marchesi et al. 2016, in preparation); the X-ray spectral analysis and X-ray variability of the bright sample with a focus on the hunt for obscured sources (G. Lanzuisi et al. 2016, in preparation); the multiwavelength spectral energy distribution fitting with host galaxy properties (mass and SF rates) for both optically classified as obscured and unobscured sources (H. Suh et al. 2016, in preparation); clustering measurement and dark matter halo mass (V. Allevato et al. 2016, in preparation); and a catalog of X-ray extended sources (Finoguenov et al. 2015, in preparation).

The wide area and the availability of extensive multi-wavelength data in the COSMOS field enable us to probe the

average X-ray emission of objects that are not individually detected by *Chandra* and therefore beyond the flux limit through a stacking analysis. The combined *Chandra COSMOS-Legacy* data set is now fully implemented in the web-based *Chandra* stacking tool CSTACK.³⁹ This enables us to investigate the X-ray properties of differently selected samples such as optical selected galaxies (e.g., Mezcuca et al. 2016, finding indications of weak AGN activity in low mass non-elliptical galaxies), highly obscured AGN selected using both infrared or radio criteria, and early AGN populations at $z > 5$.

The authors thank the referee for the useful comments. F. C. and M. C. U. gratefully thank Debra Fine for her support to women in science and the *Chandra* EPO team, in particular J. De Pasquale, for creating the true-color X-ray image. This research has made use of data obtained from the *Chandra* Data Archive and software provided by the *Chandra* X-ray Center (CXC) in the CIAO application package.

This work was supported in part by NASA *Chandra* grant number GO7-8136A (F.C., S.M., V.A., M.E., H.S.); PRIN-INAF 2014 “Windy Black Holes combing galaxy evolution” (A.C., M.B., G.L. and C.V.); the FP7 Career Integration Grant “eEASy”: “Supermassive blackholes through cosmic time: from current surveys to eROSITA-Euclid Synergies”(CIG 321913; M.B. and G.L.); UNAM-DGAPA Grant PAPIIT IN104113 and CONACyT Grant Científica Básica #179662 (T.M.); Collaborative Research Council 956, sub-project A1, funded by the Deutsche Forschungsgemeinschaft (A.K.); NASA contract NAS8-03060 (T.A., A.F., K.G.); the Greek General Secretariat of Research and Technology in the framework of the Programme of Support of Postdoctoral Researchers (P.R.); NASA award NNX15AE61G (R.G.); the Science and Technology Facilities Council through grant code ST/I001573/1 (D.M.A.); the Swiss National Science Foundation Grant PP00P2_138979/1 (K.S.); the Center of Excellence in Astrophysics and Associated Technologies (PFB 06), by the FONDECYT regular grant 1120061 and by the CONICYT Anillo project ACT1101 (E.T.); the European Union’s Seventh Framework Programme under grant agreements 337595 (ERC Starting Grant, “CoSMass”) and 333654 (CIG, AGN feedback; V.S.). S.T. is part of The Dark Cosmology Centre, funded by the Danish National Research Foundation. B.T. is a Zwicky Fellow.

REFERENCES

- Aird, J., Comastri, A., Brusa, M., et al. 2013, arXiv:1306.2325
 Allevato, V., Finoguenov, A., Cappelluti, N., et al. 2011, *ApJ*, 736, 99
 Brusa, M., Civano, F., Comastri, A., et al. 2010, *ApJ*, 716, 348
 Capak, P., Aussel, H., Ajiki, M., et al. 2007, *ApJS*, 172, 99
 Capak, P. L., Riechers, D., Scoville, N. Z., et al. 2011, *Natur*, 470, 233
 Cappelluti, N., Brusa, M., Hasinger, G., et al. 2009, *A&A*, 497, 635
 Cappelluti, N., Kashlinsky, A., Arendt, R. G., et al. 2013, *ApJ*, 769, 68
 Civano, F., Brusa, M., Comastri, A., et al. 2011, *ApJ*, 741, 91
 Civano, F., Elvis, M., Brusa, M., et al. 2012, *ApJS*, 201, 30
 Civano, F., Hickox, R. C., Puccetti, S., et al. 2015, *ApJ*, 808, 185
 Cruddace, R. G., Hasinger, G. R., & Schmitt, J. H. 1988, Scientific Objectives and Methodological Approaches in European Southern Observatory Conf. and Workshop Proc., 28, 177
 Damiani, F., Maggio, A., Micela, G., & Sciortino, S. 1997, *ApJ*, 483, 350
 Elvis, M., Civano, F., Vignali, C., et al. 2009, *ApJS*, 184, 158
 Finoguenov, A., Guzzo, L., Hasinger, G., et al. 2007, *ApJS*, 172, 182
 Fruscione, A., McDowell, J. C., Allen, G. E., et al. 2006, Proc. SPIE, 6270, 62701V
 Garmire, G. P., Bautz, M. W., Ford, P. G., Nousek, J. A., & Ricker, G. R., Jr. 2003, Proc. SPIE, 4851, 28
 Giallongo, E., Grazian, A., Fiore, F., et al. 2015, *A&A*, 578, A83
 Gilli, R., Comastri, A., & Hasinger, G. 2007, *A&A*, 463, 79
 Goulding, A. D., Forman, W. R., Hickox, R. C., et al. 2012, *ApJS*, 202, 6
 Harrison, F. A., Craig, W. W., Christensen, F. E., et al. 2013, *ApJ*, 770, 103
 Hasinger, G., Burg, R., Giacconi, R., et al. 1993, *A&A*, 275, 1
 Hasinger, G., Cappelluti, N., Brunner, H., et al. 2007, *ApJS*, 172, 29
 Hickox, R. C., & Markevitch, M. 2006, *ApJ*, 645, 95
 Ilbert, O., Capak, P., Salvato, M., et al. 2009, *ApJ*, 690, 1236
 Kalberla, P. M. W., Burton, W. B., Hartmann, D., et al. 2005, *A&A*, 440, 775
 Kettula, K., Finoguenov, A., Massey, R., et al. 2013, *ApJ*, 778, 74
 Koekemoer, A. M., Aussel, H., Calzetti, D., et al. 2007, *ApJS*, 172, 196
 Krumpe, M., Miyaji, T., Brunner, H., et al. 2015, *MNRAS*, 446, 911
 LaMassa, S. M., Urry, C. M., Cappelluti, N., et al. 2013a, *MNRAS*, 436, 3581
 LaMassa, S. M., Urry, C. M., Cappelluti, N., et al. 2015, arXiv:1510.00852
 LaMassa, S. M., Urry, C. M., Glikman, E., et al. 2013b, *MNRAS*, 432, 1351
 Lanzuisi, G., Civano, F., Elvis, M., et al. 2013, *MNRAS*, 431, 978
 Lehmer, B. D., Xue, Y. Q., Brandt, W. N., et al. 2012, *ApJ*, 752, 46
 Lilly, S. J., Le Brun, V., Maier, C., et al. 2009, *ApJS*, 184, 218
 Luo, B., Bauer, F. E., Brandt, W. N., et al. 2008, *ApJS*, 179, 19
 Lusso, E., Comastri, A., Simmons, B. D., et al. 2012, *MNRAS*, 425, 623
 Lutz, D., Poglitsch, A., Altieri, B., et al. 2011, *A&A*, 532, A90
 Mainieri, V., Bongiorno, A., Merloni, A., et al. 2011, *A&A*, 535, A80
 Marchesi, S., Civano, F., Elvis, M., et al. 2016, *ApJ*, 817, 34
 Mateos, S., Warwick, R. S., Carrera, F. J., et al. 2008, *A&A*, 492, 51
 McCracken, H. J., Milvang-Jensen, B., Dunlop, J., et al. 2012, *A&A*, 544, A156
 Merloni, A. 2012, Science from the Next Generation Imaging and Spectroscopic Surveys, 43
 Mezcuca, M., Civano, F., Fabbiano, G., Miyaji, T., & Marchesi, S. 2016, *ApJ*, 817, 20
 Murray, S. S., Kenter, A., Forman, W. R., et al. 2005, *ApJS*, 161, 1
 Nandra, K., Barret, D., Barcons, X., et al. 2013, arXiv:1306.2307
 Nandra, K., Laird, E. S., Aird, J. A., et al. 2015, arXiv:1503.09078
 Park, T., Kashyap, V. L., Siemiginowska, A., et al. 2006, *ApJ*, 652, 610
 Pierre, M., Valtchanov, I., Altieri, B., et al. 2004, *JCAP*, 9, 011
 Puccetti, S., Vignali, C., Cappelluti, N., et al. 2009, *ApJS*, 185, 586
 Ranalli, P., Georgantopoulos, I., Corral, A., et al. 2015, *A&A*, 577, A121
 Schinnerer, E., Carilli, C. L., Scoville, N. Z., et al. 2004, *AJ*, 128, 1974
 Schinnerer, E., Sargent, M. T., Bondi, M., et al. 2010, *ApJS*, 188, 384
 Schinnerer, E., Smolčić, V., Carilli, C. L., et al. 2007, *ApJS*, 172, 46
 Scoville, N., Abraham, R. G., Aussel, H., et al. 2007a, *ApJS*, 172, 38
 Scoville, N., Aussel, H., Brusa, M., et al. 2007b, *ApJS*, 172, 1
 Smolčić, V., Ciliegli, P., Jelić, V., et al. 2014, *MNRAS*, 443, 2590
 Taniguchi, Y., Scoville, N., Murayama, T., et al. 2007, *ApJS*, 172, 9
 Trakhtenbrot, B., Urry, C. M., Civano, F., et al. 2015, *Sci*, 349, 168
 Treister, E., Urry, C. M., & Virani, S. 2009, *ApJ*, 696, 110
 Vikhlinin, A., Reid, P., Tananbaum, H., et al. 2012, Proc. SPIE, 8443, 844316
 Weisskopf, M. C., Brinkman, B., Canizares, C., et al. 2002, *PASP*, 114, 1
 Wilkes, B. J., Kilgard, R., Kim, D.-W., et al. 2009, *ApJS*, 185, 433
 Wilkes, B. J., Kuraszkiewicz, J., Haas, M., et al. 2013, *ApJ*, 773, 15
 Xue, Y. Q., Luo, B., Brandt, W. N., et al. 2011, *ApJS*, 195, 10

³⁹ See <http://lambic.astro.unam.mx/cstack>. Login as user—guest with password—guest and see the explanatory manual. As of writing this paper, stacking analyses utilizing the C-COSMOS data set is publicly available. Analyses involving the whole *Chandra COSMOS-Legacy* data set is still proprietary and will be public in due course.